



**HAL**  
open science

## Initiation of immersed granular avalanches

Patrick Mutabaruka, Jean-Yves Delenne, Kenichi Soga, Farhang Radjai

► **To cite this version:**

Patrick Mutabaruka, Jean-Yves Delenne, Kenichi Soga, Farhang Radjai. Initiation of immersed granular avalanches. *Physical Review E: Statistical, Nonlinear, and Soft Matter Physics*, 2014, 89 (5), 10.1103/PhysRevE.89.052203 . hal-02093034

**HAL Id: hal-02093034**

**<https://hal.science/hal-02093034v1>**

Submitted on 8 Apr 2019

**HAL** is a multi-disciplinary open access archive for the deposit and dissemination of scientific research documents, whether they are published or not. The documents may come from teaching and research institutions in France or abroad, or from public or private research centers.

L'archive ouverte pluridisciplinaire **HAL**, est destinée au dépôt et à la diffusion de documents scientifiques de niveau recherche, publiés ou non, émanant des établissements d'enseignement et de recherche français ou étrangers, des laboratoires publics ou privés.

## Initiation of immersed granular avalanches

Patrick Mutabaruka,<sup>1,\*</sup> Jean-Yves Delenne,<sup>2,†</sup> Kenichi Soga,<sup>3,‡</sup> and Farhang Radjai<sup>4,5,§</sup>

<sup>1</sup>LMGC, UMR 5508, Université Montpellier 2, CNRS, Place E. Bataillon, 34095 Montpellier, France

<sup>2</sup>IATE, UMR1208, INRA, University Montpellier 2, Cirad, SupAgro, 34060 Montpellier, France

<sup>3</sup>Cambridge University, Engineering Department, Cambridge CB2 1PZ, United Kingdom

<sup>4</sup>University Montpellier 2, CNRS, LMGc, Place E. Bataillon, 34095 Montpellier, France

<sup>5</sup>Laboratoire de Micromécanique et Intégrité des Structures (MIST), CNRS, IRSN, Université Montpellier 2, France

(Received 31 October 2013; published 9 May 2014)

By means of coupled molecular dynamics–computational fluid dynamics simulations, we analyze the initiation of avalanches in a granular bed of spherical particles immersed in a viscous fluid and inclined above its angle of repose. In quantitative agreement with experiments, we find that the bed is unstable for a packing fraction below 0.59 but is stabilized above this packing fraction by negative excess pore pressure induced by the effect of dilatancy. From detailed numerical data, we explore the time evolution of shear strain, packing fraction, excess pore pressures, and granular microstructure in this creeplike pressure redistribution regime, and we show that they scale excellently with a characteristic time extracted from a model based on the balance of granular stresses in the presence of a negative excess pressure and its interplay with dilatancy. The cumulative shear strain at failure is found to be  $\simeq 0.2$ , in close agreement with the experiments, irrespective of the initial packing fraction and inclination angle. Remarkably, the avalanche is triggered when dilatancy vanishes instantly as a result of fluctuations while the average dilatancy is still positive (expanding bed) with a packing fraction that declines with the initial packing fraction. Another nontrivial feature of this creeplike regime is that, in contrast to dry granular materials, the internal friction angle of the bed at failure is independent of dilatancy but depends on the inclination angle, leading therefore to a nonlinear dependence of the excess pore pressure on the inclination angle. We show that this behavior may be described in terms of the contact network anisotropy, which increases with a nearly constant connectivity and levels off at a value (critical state) that increases with the inclination angle. These features suggest that the behavior of immersed granular materials is controlled not only directly by hydrodynamic forces acting on the particles but also by the influence of the fluid on the granular microstructure.

DOI: [10.1103/PhysRevE.89.052203](https://doi.org/10.1103/PhysRevE.89.052203)

PACS number(s): 45.70.-n, 61.43.-j, 47.57.Gc

### I. INTRODUCTION

Mixtures of granular materials with water are major ingredients of natural processes such as erosion, sediment transport and deposit, landslides, slope failure, and submarine avalanches [1–7]. In the same way, particle-laden fluids are fundamental in operations such as oil recovery and wet processing in powder technology and the food and pharmaceutical industries [8]. The interaction of fluid with solid particles leads to novel effects combining the complex density-dependent, pressure-sensitive, and anisotropic behavior of granular materials with the inertial, viscous, capillary, and lubricating forces of the fluid acting on the particle phase through the pore space.

From the viewpoint of non-Brownian suspensions, the central concern is how the suspended particles affect the fluid behavior as a function of their concentration in different flow regimes [9,10]. Most research in this field is therefore based on volume-controlled rheometry with isodense particles, and mechanical contacts between particles are often neglected. In the case of immersed granular materials, however, the limit of high particle concentration is governed by frictional contact interactions and the query is rather how the fluid affects granular flow [11–13].

A key feature of the dense regime is the Reynolds dilatancy. Granular flows occur at a constant mean packing fraction  $\nu^*$  in the steady state (critical state in soil mechanics; e.g., Ref. [14]). This packing fraction depends on the material but also on the confining stress and shear rate. When the packing fraction  $\nu$  differs from  $\nu^*$ , shear deformation is accompanied by volume change and  $\nu$  tends to  $\nu^*$  [15–17]. Hence, the evolution of the shear stress during this transient is crucially dependent on the initial packing state. In the presence of an ambient fluid, the expansion or contraction of the packing occurs with a relative motion of the grains with respect to the fluid, which tends thus to develop negative or positive excess pressure, respectively, in the pore space, affecting in turn the deformation. The magnitude of excess pore pressure depends on the diffusion rate of pore pressure associated with pore water flow [18–20].

This strong coupling between dilatancy and pore pressure is vital for the onset of flow but also under all kind of complex loading such as cyclic shearing or changes of the confining load [16]. The seminal large-scale experiments of Iverson *et al.* clearly evidenced this effect by watering samples of soil prepared with different packing fractions and inclined above their angle of repose [21]. The dense samples were shown to creep slowly down the slope, whereas the loose samples underwent sudden slope failure. The effect of the initial packing fraction was later investigated by means of laboratory experiments by Pailha *et al.* on samples of granular materials fully immersed in liquids of different viscosities and inclined to different angles [19]. The authors were able to address quantitatively the effect of dilatancy on the avalanche

\*patrick.mutabaruka@univ-montp2.fr

†delenne@supagro.inra.fr

‡ks207@cam.ac.uk

§franck.radjai@univ-montp2.fr

initiation and proposed a modeling approach based on the stress balance and Darcian drag force. In particular, they found that the slope failure in dense samples occurs always for a nearly constant shear deformation ( $\simeq 0.25$ ), which may be used as criterion to predict the time delay before slope failure. Hence, assuming that failure occurs at shear deformation 0.25, they were able to scale the experimental data regarding the triggering time as a function of the initial packing fraction.

The experimental results cited above raise, however, several basic questions as to the effect of fluid. In particular, the avalanche threshold in the dense case is found to be independent of dilatancy. This is unexpected since the avalanche threshold in dry granular materials reflects both the internal friction coefficient of the material and its dilatancy, which is an increasing function of the initial packing fraction [22]. In fact, in the soil mechanics literature, the failure threshold of a dense granular material is attributed to the “peak” friction coefficient, which increases with the peak dilatancy, but it declines towards the steady friction coefficient in the “critical state” after failure, i.e., when dilatancy vanishes [15,16]. Assuming chemically inert particles, this mechanical behavior is expected to be the same under dry and immersed conditions. It is also important to note that the total shear strain required to reach the peak state is a decreasing function of the packing fraction. This picture contradicts the experimental observation that the avalanche is always triggered at nearly the same shear strain of 0.25 [19].

In this paper, we present a novel investigation of the initiation of granular avalanches inside a viscous fluid by means of three-dimensional (3D) simulations. The numerical simulation of fluid-grain mixtures is a challenging issue that requires the joint integration of the equations of motion of the grains and fluid [23–29]. For this reason, coupled simulations hardly begin to be used as an investigation tool for dense granular materials in a fluid. However, when possible, the simulations have the advantage of providing access to the spatiotemporal evolution of the system at both large and small scales.

As we shall see below, our systematic numerical simulations with appropriate boundary conditions reproduce well all experimental results in the whole process of destabilization of a granular bed inclined above its angle of repose. They allow us to go beyond experiments and explore the distribution of fluid pressures and grain velocities as well as the evolution of the contact network for different values of the initial packing fraction and three values of the inclination angle. An interesting finding of this work is that the contact network deforms mainly by distortion at a nearly constant coordination number. This is a genuine deformation mechanism that has not been observed previously, and it indicates why the avalanche threshold is independent of dilatancy. We also extend the theoretical model introduced by Iverson *et al.* [30] and adapted to rigid grains by Pailha *et al.* [19] in order to predict the time evolution of the shear strain and packing fraction. The numerical data are found to be in excellent agreement with this model, and they provide direct evidence for the assumptions underlying the model.

In the following, we first describe our numerical approach and system parameters. In Sec. III, we present the spatiotemporal evolution of the system as a function of the initial packing fraction. Then, in Sec. IV, we focus on the creep regime.

In Sec. V, we introduce a reformulation of the theoretical model and compare its predictions with our simulation data. In Sec. VI, we investigate the evolution of the contact network and introduce a simple model for the relation between the contact anisotropy and internal friction. We conclude with a summary and brief discussion of the main findings of this work.

## II. NUMERICAL PROCEDURES

The discrete-element method (DEM) for the simulation of granular systems with frictional contact interactions is already a mature tool that is applied in conjunction with experiments both for a better understanding of the micromechanics of granular materials and as a means of “virtual” experimentation when laboratory experiments are unavailable [31]. In a similar vein, the inclusion of a fluid at the subgranular scale in DEM simulations provides a powerful tool in the broad field of fluid-grain mixtures. Obviously, the available computational power and research time restrict considerably the number of tractable grains. In the case of dry granular materials, statistically representative samples are obtained and simulated with  $N \times 10^4$  of grains in 2D. Despite enhanced kinematic constraints, 2D simulations often lead to novel physical insights and realistic behaviors that can be easily generalized to 3D configurations. However, with fluid in the pore space, 2D simulations are much less reliable in the dense regime since the pore space is discontinuous with zero permeability. This two-dimensional flaw can be partially repaired by adding artificially a permeable layer on the particles. But only 3D simulations may account for a realistic behavior of grain-fluid mixtures with their natural permeability.

We developed a 3D fluid dynamics algorithm based on the lattice Boltzmann method (LBM). This algorithm was interfaced with a DEM algorithm with a standard linear spring-dashpot model of contact between grains. A brief account of the LBM is given in Appendix A. The simulation cell is a cuboidal domain of height  $H_f$  and square section of side  $L$ , to which a coordinate system  $(x, y, z)$  is attached, as shown in Fig. 1. The cell is filled by  $N_s$  spherical grains up to a height  $H_s$  and a fluid to the full height  $H_f$ . Periodic boundary conditions are implemented along the  $x$  and  $y$  directions for both fluid and grains. The cell represents thus a volume element of a granular bed extending to the infinity along the  $x$  and  $y$  directions. The bottom wall is made rough by a layer of immobile grains. The no-slip condition is imposed on the fluid at bottom walls as well as at the grain-fluid interface and a Dirichlet condition at the top for fluid. The gravity  $g$  acts vertically both on the grains and fluid. The box is instantly tilted at an angle  $\theta$  with respect to the horizontal in the  $xz$  plane. The grains start to flow under the action of their own weights and in interaction with the fluid along the  $x$  direction.

The grains have a density  $\rho_s = 2600 \text{ kg/m}^3$ , corresponding to that of rock debris, and a uniform size distribution between  $d_{\min}$  and  $d_{\max}$  with  $d_{\max} = 1.33d_{\min}$ . The mean grain diameter is  $d = 6.9 \times 10^{-4} \text{ m}$ . The friction coefficient between grains and with the bottom wall is set to  $\mu_s = 0.4$ . With these parameters, the angle of repose is  $\theta_r \simeq 22^\circ$ , but the internal friction angle  $\varphi^*$  depends also on the slope  $\theta$ , as we shall see below. The fluid density is fixed to  $\rho_f = 1000 \text{ kg/m}^3$  and

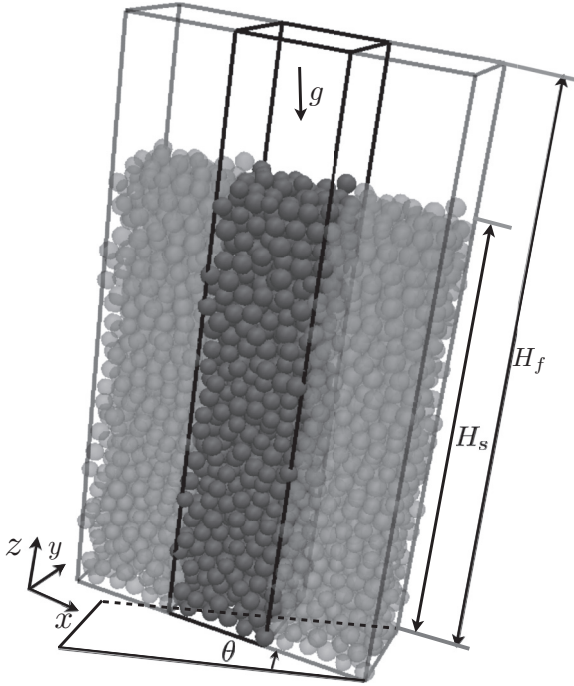


FIG. 1. Simulation cell with periodic boundary conditions.

all simulations reported in this paper were carried out with a single fluid viscosity  $\eta = 0.025$  Pa s.

Several granular samples were first prepared without fluid with different initial values of the packing fraction  $\nu_0$  inside the simulation cell by using the following procedure. A dense packing is first constructed by allowing a gas of grains to fall into the cell with zero friction coefficient between the grains. This leads to a packing fraction  $\nu \simeq 0.63$ . The friction coefficient is then set to  $\mu_s$  and a number of randomly selected grains are removed successively from the packing, which is allowed to relax to equilibrium after each grain removal. The evolution of the packing fraction is composed of a series of partial compaction events but, since the initial packing is dense, this process leads to a gradual decrease of the packing fraction down to 0.56. Figure 2 displays the evolution of  $\nu$  during this process as a function of the number of grains removed.

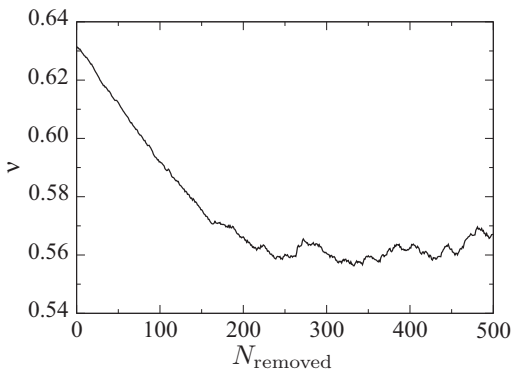


FIG. 2. Evolution of the packing fraction as a function of the number of grains removed from the simulation cell.

Samples with different values of the initial packing fraction are then constructed from different steps of the evolution of the packing by removing all the grains lying above  $H_s$ . The number of grains  $N_s$  varies from 872 to 974 for  $\nu_0$  varying from 0.56 to 0.63. The resulting granular bed has the desired packing fraction, a flat surface (with variability of the order of one grain diameter), and periodic boundaries along the  $x$  and  $y$  directions.

The granular bed prepared by the above method on a horizontal bottom is tilted at an angle  $\theta$  in the positive  $x$  direction. This is strictly equivalent to the rotation of the direction of gravity to the same angle with its components  $g \sin \theta$  and  $g \cos \theta$  acting along and perpendicular to the granular bed, respectively. The component  $g \cos \theta$  gives rise to a normal stress  $\sigma_{zz}^h = (\rho_s - \rho_f) \nu g (H_s - z) \cos \theta$ , increasing with depth in the  $z$  direction, whereas periodicity along the  $x$  direction cancels the stress gradients in the direction of flow so the normal stress  $\sigma_{xx}$  and shear stress  $\sigma_{zx}$  are independent of  $x$ . For the same reason, all stress components are invariant along the  $y$  direction. The system can thus be analyzed in terms of averaged observables in volume elements parallel to the  $xy$  plane as a function of  $z$  and time  $t$ .

The periodic boundary conditions play an important role in this work not only by providing homogeneous conditions along  $x$  and  $y$  directions but also by making it possible to perform 3D fluid-grain simulations with a rather small number of grains, imposed by the high computational cost of the integration of a large number of fluid degrees of freedom. However, since the system is not periodic along the  $z$  direction, the bed should be high enough in number of grain diameters for the stress and velocity gradients to be fully expressed. As we shall see below, this condition is fulfilled with  $H_s \simeq 25d$ , which was used in our simulations. At the same time, in order to limit the total number of grains to  $N_s < 1000$  for a reasonable simulation time, the width of the cell was fixed to  $L \simeq 6d$ , which is clearly not wide enough to prevent finite-size effects. In practice, however, the flow of the grain-fluid mixture is well behaved and our data are consistent with experimental results. The goal of this work was not to carry out a single simulation of a large system, which would have been an interesting achievement in high-performance computation but rather to analyze the initiation of immersed granular avalanches in a quantitative manner and for different values of the relevant physical parameters. The data presented in this paper correspond to a single run for each set of parameters (inclination angle and initial packing fraction).

The numerical parameters were fixed as a trade-off between efficiency and precision. We set the normal contact parameters to  $k_n = 10^6$  N/m and  $\gamma_n = 0.57$  N s m<sup>-1</sup>; see Appendix A. The normal restitution coefficient with these parameters is  $\simeq 0.2$ . For the tangential parameters, we set  $k_t = 0.8k_n$ , which is a common value in DEM simulations. But in order to avoid undesired interplay between the fluid viscosity  $\eta = 0.025$  Pa s and the tangential contact damping viscosity parameter  $\gamma_t$  during shear, we set  $\gamma_t = 0$ . We performed several preliminary simulations with different values of these parameters. We found that large values of  $\gamma_t$  mask partially the effect of fluid viscosity whereas the value of  $\gamma_n$  is indifferent. It is worth noting that low-frequency elastic waves in the granular packing are efficiently damped by fluid drag forces, with the effect of increasing the stability of DEM calculations.

The lattice spacing for LBM calculations was fixed to  $\delta x = d/10$ . This choice was checked in several configurations in which the trajectories of a single grain in a fluid were compared to the available theoretical predictions (free fall, simple shear, collision between two grains). Finally, we also checked that the lubrication forces were correctly expressed between two colliding grains at distances as small as the LBM mesh. At such scales, the LBM mesh plays the same role as natural asperities at the surface of a grain, allowing thus for mechanical contact between two grains. The LBM time step was set to  $\delta t_{\text{LBM}} = 2.3 \times 10^{-5}$  s from the lattice velocity  $c = 3$  and the lattice spacing  $\delta x = d/10$ ; see Appendix A. The DEM time step was  $\delta t_i = 10^{-7}$  s. This means that the hydrodynamic forces acting on the grains do not evolve during 230 DEM time steps. In fact, as we will see, the physical time scales involved in the process of slope failure and its consecutive dynamics are well above  $\delta t_{\text{LBM}}$  so the evolution of the fluid is not significant at the scale of the smooth and slow DEM time stepping, which is necessary for the resolution of elastic waves. Note also that, for our  $10^3$  grains, the 230 DEM steps take less time than a single LBM step due to the large number of fluid nodes. Video samples of the simulations analyzed in this paper can be found by following the link provide in Ref. <http://www.cgp-gateway.org/ref026>.

### III. SPATIOTEMPORAL EVOLUTION

In this section, we give a general description of the evolution of the system from our numerical data. A detailed analysis is then performed in the creep regime in Sec. IV and a theoretical model is presented in Sec. V.

Figure 3 displays snapshots of the contact network, grain velocities  $\vec{v}^i$ , and fluid excess pressures  $p_f(\vec{r})$  in the cell frame in an initially dense system. A marked gradient of grain velocities and pore pressures is observed along the  $z$  direction. We consider volume-averaged grain and fluid velocities  $v_x(z)$  and  $v_y(z)$  and fluid excess pressures  $p_f(z)$  defined within each

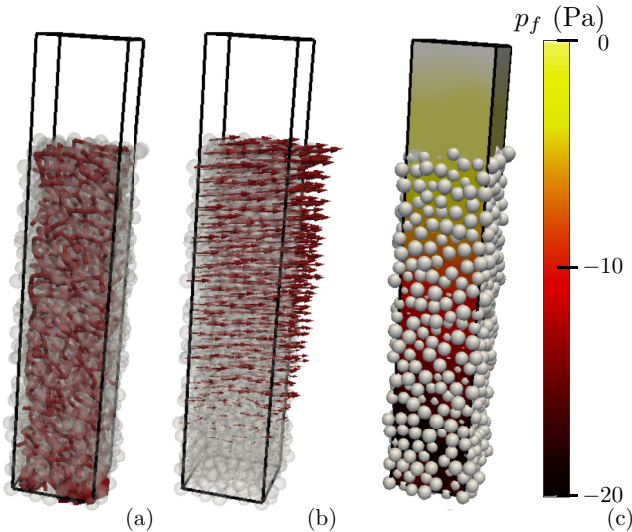


FIG. 3. (Color online) Snapshot of the contact network, grain velocities and excess fluid pressures during the creeplike motion of an immersed granular slope.

horizontal slice of thickness  $\Delta z = 4d$  and center located at height  $z$ . The mean strain rates are given by

$$\dot{\varepsilon}_{zx} = \frac{v_x(H_s)}{H_s}, \quad (1)$$

$$\dot{\varepsilon}_{zz} = -\frac{v_z(H_s)}{H_s}, \quad (2)$$

from which the cumulative strains  $\varepsilon_{zx}$  and  $\varepsilon_{zz}$  are obtained by integration over time as follows:

$$\varepsilon_{zx}(t) = \int_0^t \dot{\varepsilon}_{zx}(t') dt', \quad (3)$$

$$\varepsilon_{zz}(t) = \int_0^t \dot{\varepsilon}_{zz}(t') dt'. \quad (4)$$

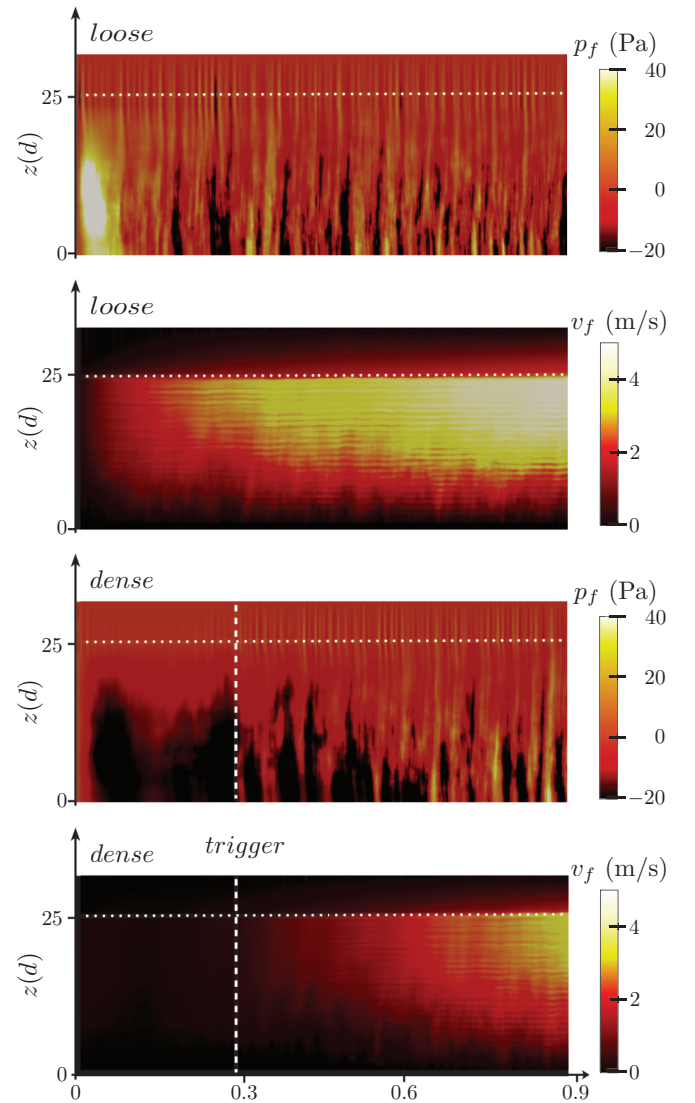


FIG. 4. (Color online) Spatiotemporal evolution of velocities and fluid excess pressures in the the loose and dense regimes for  $\theta = 26^\circ$ . The dotted lines indicate the top surface of the bed. In the dense regime, the trigger time is indicated by a vertical dashed line.

The mean dilatancy angle  $\psi$  is defined by

$$\tan \psi = -\frac{\dot{\epsilon}_{zz}}{\dot{\epsilon}_{zx}}. \quad (5)$$

Figure 4 shows the spatiotemporal diagrams of  $v_x$  and  $p_f$  for an initially loose bed with initial packing fraction  $\nu_0 = 0.57$  and an initially dense bed with  $\nu_0 = 0.63$ . The origin of time is when the bed is tilted at  $\theta = 26^\circ$ . In the loose case, starting with zero grain and fluid velocities, the bed is unstable from the very beginning with a destabilization front propagating rapidly from the free surface towards the bottom. The grains are accelerated with a positive upward gradient. The fluid above the bed is driven by the granular bed, but the induced shear velocity is small and it declines towards the upper cell wall. The large positive fluid excess pressure appearing in the fluid indicates that the grains are partially suspended by the fluid. Indeed, the packing fraction being low, the bed has to contract during shear deformation. The negative dilatancy implies the expulsion of fluid from the pores, leading thus to a positive excess pressure that affects the bed by reducing the normal and friction forces between the grains. This positive pore pressure feedback is a well-known mechanism that may cause slope liquefaction after intense rainfalls [5,30,32]. Interestingly, although the large positive excess pressure built up at the beginning of failure disappears with time, we still observe bursts of large positive or negative excess pressure as the avalanche develops. Such events start both at the free surface and slightly above the bottom wall, and they reflect the microinstabilities occurring during shear deformation of granular materials. The bursts indicate that such fluctuations are enhanced by interaction with fluid.

In the dense case, the bed remains stable for a while with very weak creeping velocities after inclination. The slope failure occurs around  $t \simeq 0.28$  s with nearly the whole bed destabilized except the lowest layers, which begin to flow later. The spatiotemporal diagram shows the buildup of a negative excess pressure increasing from the free surface towards the bottom. In contrast to the loose case, the bed has dilative tendency during shear deformation. As a result, the fluid is sucked into the pores with time, leading to the negative excess pore pressure and increase of the normal and friction forces between the grains. But at the same time the negative excess pressure starts to dissipate as the fluid is sucked into the pores. This in turn reduces the normal and frictional forces between the grains. Hence, the bed remains stable but creeps slowly as long as dilation continues. As in the loose case, we observe bursts of negative and positive excess pressures during the avalanche after failure.

To characterize the effect of  $\nu_0$  on the evolution of the granular bed, we show in Fig. 5 the center-of-mass velocity  $v_x^{c.m.} \simeq v_x(H_s/2)$  of the grains and the packing fraction  $\nu$  as a function of time for  $\theta = 26^\circ$  and eight different values of  $\nu_0$  in the range  $[0.56, 0.63]$ . We clearly distinguish two regimes: (1) For  $\nu \leq 0.59$  (loose regime), the center-of-mass velocity increases monotonically at an increasingly higher rate as  $\nu_0$  decreases. The packing fraction increases, passes by a peak value, and then declines. (2) For  $\nu > 0.59$  (dense regime), the center-of-mass velocity keeps a small nearly constant value until slope failure is triggered with a sudden increase of the velocity. The triggering time  $t^{\text{trig}}$  increases with  $\nu_0$ .

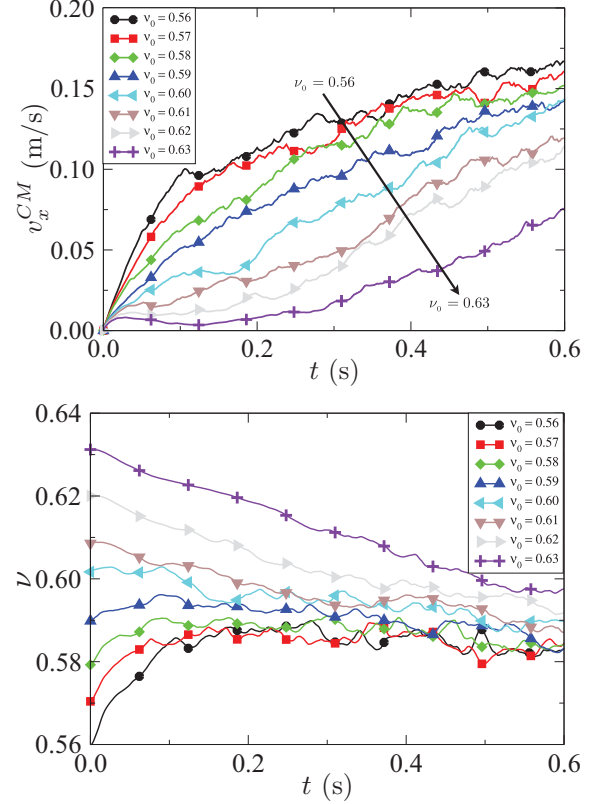


FIG. 5. (Color online) Center-of-mass velocity  $v_x^{c.m.}$  along  $x$  and packing fraction  $\nu$  as a function of time for different values of the initial packing fraction  $\nu_0$ .

The packing fraction declines at a constant rate with time. It continues to decrease at a lower rate after slope failure. A steady state is reached with a nearly constant velocity and packing fraction at  $t \simeq 1.5$  s.

The transition packing fraction 0.59 is very close to that found also in the experiments of Pailha *et al.* [19] and Rondon *et al.* [20], as well as in dry granular media for transition from the contracting regime to the dilating regime [33]. However, its value should naturally depend on the particle properties such as particle shape and size distribution and solid friction between particles.

Figure 6 shows the fluid excess pressure  $p_f(z=0)$  at the bottom ( $z=0$ ) of the bed and the mean dilatancy  $\tan \psi$  for several values of  $\nu_0$  and  $\theta = 26^\circ$ . In the loose cases, a large positive excess pressure builds up immediately after inclination and, up to fluctuations, it declines rapidly and vanishes on average during flow. Its peak value is higher at lower packing fractions. The dilatancy angle is negative, corresponding to the contraction of the bed, and it declines in absolute value and vanishes in correlation with pore pressure. In the dense cases, a negative excess pressure builds up together with a positive dilatancy angle, corresponding to the expansion of the bed. The pore excess pressure keeps a nearly constant value, and it begins to decline only after slope failure.

The fluctuations in the dense cases reveal the very fragile nature of the mechanical equilibrium during creeplike deformation of the bed, making it difficult to assess precisely the exact triggering time from the times series of packing

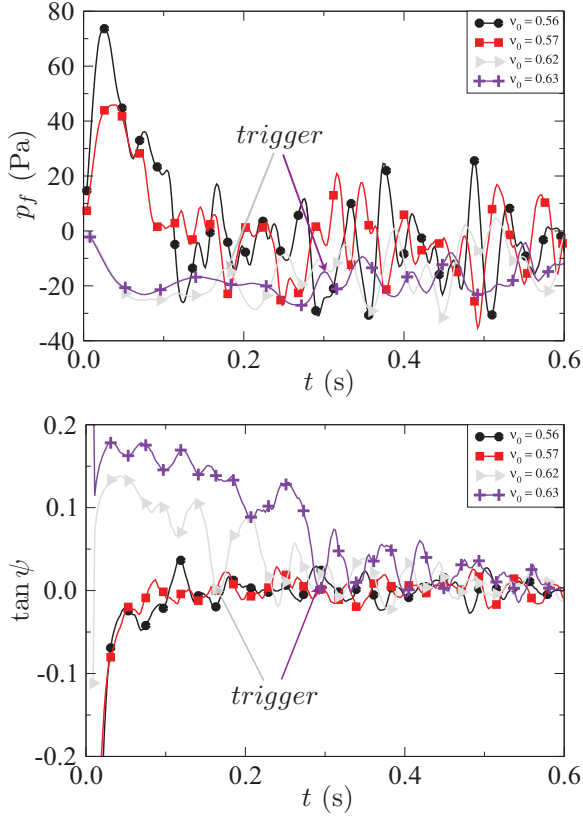


FIG. 6. (Color online) Fluid excess pressure  $p_f(z = 0)$  at the bottom of the bed and the mean bed dilatancy  $\tan \psi$  as a function of time for several values of the initial packing fraction and for  $\theta = 26^\circ$ .

fraction and velocities. However, by comparing the correlative evolutions of several variables, including microstructural quantities, we find that the failure is triggered as soon as the dilatancy angle  $\psi$  becomes zero for the first time. These events are marked by arrows in Fig. 6 for  $v_0 = 0.62$  and  $v_0 = 0.63$ . The same figure shows also that  $p_f(z = 0)$  undergoes a sudden decrease at the same time, leading thus to abrupt destabilization of the bed. It is remarkable that, despite this instant vanishing of  $\psi$ , its average value is positive due to fluctuations when the avalanche is triggered. For this reason, the condition of the *average* dilatancy to be zero cannot be used as a trigger criterion. Instead, we use the instant zeroing of  $\psi$  to determine the exact trigger time  $t^{\text{trig}}$  of avalanches. The packing fraction  $v^{\text{trig}}$  at failure is the packing fraction at time  $t = t^{\text{trig}}$ .

The effect of bed angle  $\theta$  is displayed in Fig. 7 where  $v_x^{c.m.}$ ,  $v$ , and  $p_f(z = 0)$  are plotted for the same packing with  $v_0 = 0.63$  as a function of time for  $\theta = 24^\circ$ ,  $26^\circ$ , and  $28^\circ$ . The creep motion lasts longer at lower  $\theta$  with  $v$  decreasing at a lower rate. The negative pore pressure increases with  $\theta$ . The terminal packing fraction  $v^*$  in the steady-state flow is of the order of 0.58 for  $\theta = 24^\circ$ , but it becomes smaller with increasing  $\theta$ . This is consistent with the larger value of the inertial number  $I$  in inertial granular flows on an inclined plane for larger  $\theta$  [20,34–38]. The inertial number is the ratio of the collision time to the shear time,

$$I(z) = \dot{\epsilon}_{zx} \sqrt{\frac{m}{\sigma_{zz}(z)d}}, \quad (6)$$

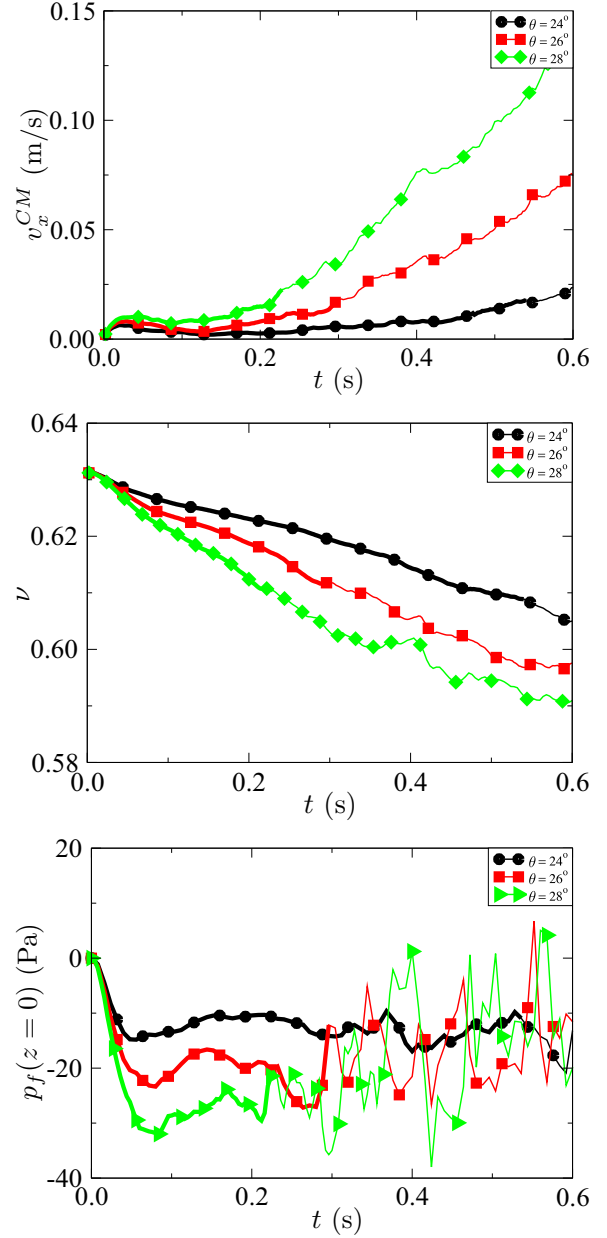


FIG. 7. (Color online) Center-of-mass velocity  $v_x^{c.m.}$ , packing fraction  $v$ , and fluid excess pressure  $p_f(z = 0)$  as a function of time for three different inclination angles. Thick lines represent the creeping part of each time series.

where  $m$  is the mean particle mass. It depends on the height  $z$  through the vertical stress  $\sigma_{zz}$ . In our simulations, the largest value of  $I$  in the creeplike regime is 0.003 for the topmost layer of the bed inclined at  $\theta = 28^\circ$ .

#### IV. CREEPLIKE PERIOD

In this section, we focus on the creeplike period during which excess pore pressure develops as shear deformation evolves and, at the same time, tends to dissipate to reach equilibrium. We are interested in the quantitative effects of the bed angle  $\theta$  and initial packing fraction  $v_0$  on the avalanche initiation and in the depth dependence of velocities and pore

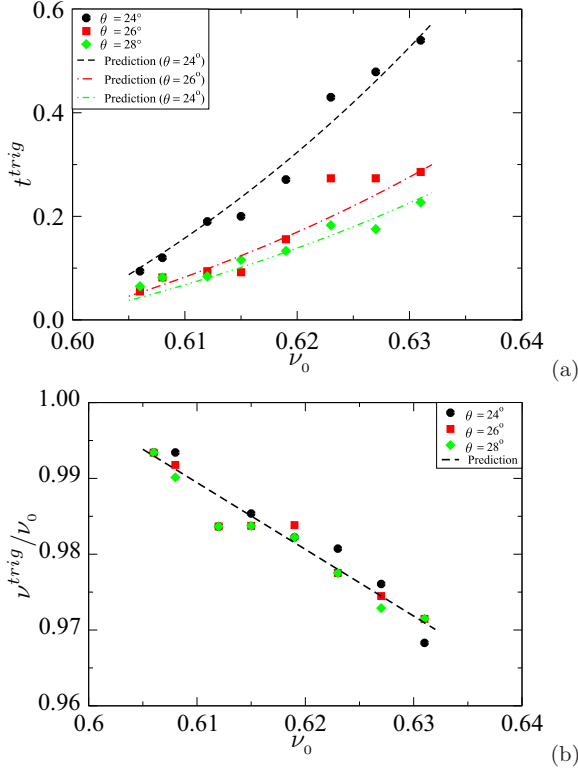


FIG. 8. (Color online) Triggering time  $t^{\text{trig}}$  and the normalized packing fraction  $\nu^{\text{trig}}/\nu_0$  at slope failure (symbols) as a function of the initial packing fraction  $\nu_0$  for different slope angles  $\theta$ . The predictions of the continuum model are represented by dashed lines.

pressures averaged over the creeplike period that represent the main ingredients of the continuum model presented in the next section.

Figure 8(a) shows the triggering time  $t^{\text{trig}}$  as a function of  $\nu_0$  ( $\geq 0.6$ ) for three values of  $\theta$ . As detailed in the last section,  $t^{\text{trig}}$  is the exact time dilatancy becomes zero for the first time. We see that  $t^{\text{trig}}$  is an increasing function of  $\nu_0$ , and for each value of  $\nu_0$ , it is longer at lower  $\theta$ . The figure shows also the predictions of the continuum model described in Sec. V. Figure 8(b) displays the packing fraction  $\nu^{\text{trig}}$  at failure as a function of  $\nu_0$  together with the theoretical prediction.  $\nu^{\text{trig}}$  increases from 0.6 to 0.61 for  $\nu_0$  increasing from 0.6 to 0.63. Note that these values of  $\nu^{\text{trig}}$  are above  $\nu^*$ . This means that slope failure does not occur for a particular value of  $\nu$ . As it is classically known from compression tests on dense soils, the hardening behavior occurs simultaneously with dilation [16,39]. Hence, although the granular slope is increasingly fragilized by the gradual decrease of  $\nu$  and increasing volume of fluid in the pores, it cannot be used as an “internal parameter” to predict the failure. We either should prescribe  $\nu^{\text{trig}}$  for given system parameters ( $\nu_0$ ) for the prediction of other quantities at failure such as triggering time or, conversely, predict  $\nu^{\text{trig}}$  from system parameters by means of a different failure criterion.

In their experiments, Pailha *et al.* [19] found that the cumulative shear strain  $\varepsilon_{zx}^{\text{trig}}$  at failure is nearly independent of  $\nu_0$  and approximately equal to 0.25. In Fig. 9 we have plotted  $v_x^{\text{c.m.}}$  as a function of  $\varepsilon_{zx}$  for different values of  $\nu_0$  and  $\theta$ . We

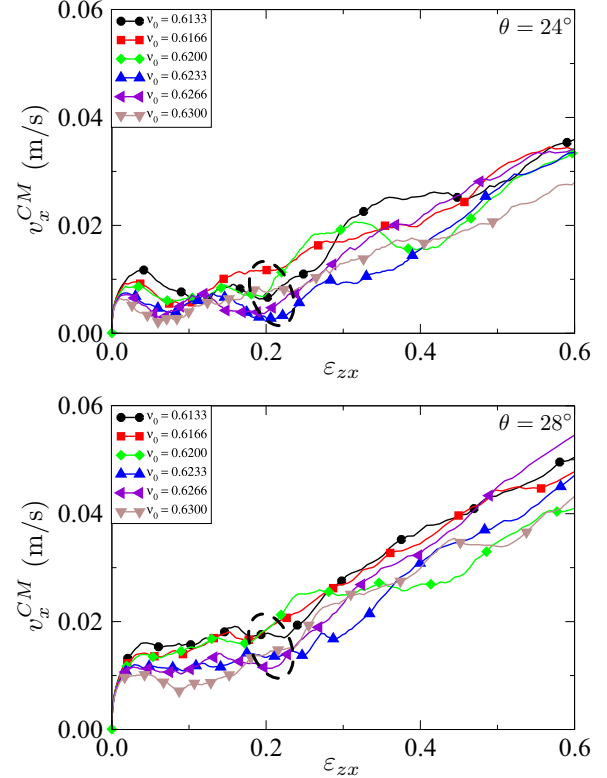


FIG. 9. (Color online) Center-of-mass velocity  $v_x^{\text{c.m.}}$  as a function of cumulative shear strain for  $\theta = 24^\circ$ ,  $\theta = 28^\circ$  and different values of  $\nu_0$ . The shear strains at failure are indicated by an ellipse.

see that  $\varepsilon_{zx}^{\text{trig}}$  increases from 0.18 to 0.22 as  $\nu_0$  is changed from 0.6 to 0.63 for all values of  $\theta$ . This variation of  $\varepsilon_{zx}^{\text{trig}}$  is small enough to allow us to use  $\varepsilon_{zx}^{\text{trig}} \simeq 0.2$  as a failure criterion. It is not, however, evident why this particular value, which is very close to the experimental value of 0.25, should be independent of  $\nu_0$ . In soil compression tests, the total shear deformation at the stress peak strongly depends on the initial packing fraction [16]. Therefore, comparing the creeplike deformation to the shear deformation before stress peak in a compression test, one expects the shear strain at failure to decrease for increasingly higher packing fraction  $\nu_0$ . What we observe here is that the same shear deformation occurs for all  $\nu_0$  and  $\theta$  but at an increasingly lower rate as  $\nu_0$  is increased. Hence, the complex interaction of shear-induced excess pore pressure and its dissipation needs to be considered to understand this observation. This discrepancy will be discussed in Sec. VI in the light of microstructural data.

A related issue is whether the creeplike deformation and slope failure occur homogeneously in the whole bed. Figure 10(a) displays the shear velocity  $v_x(z)$  for  $\nu_0 = 0.63$  and  $\theta = 26^\circ$  as a function of time for several values of  $z$ . As also shown in spatiotemporal diagrams shown in Fig. 4, we observe here a velocity gradient from the bottom towards the free surface during the creeplike period, and the avalanche is triggered at nearly the same time in the whole packing in exception to the lowermost layer where the failure is delayed. Figure 10(b) shows the excess pore pressures for the same values of  $z$ . We see a clear gradient of the excess pressure



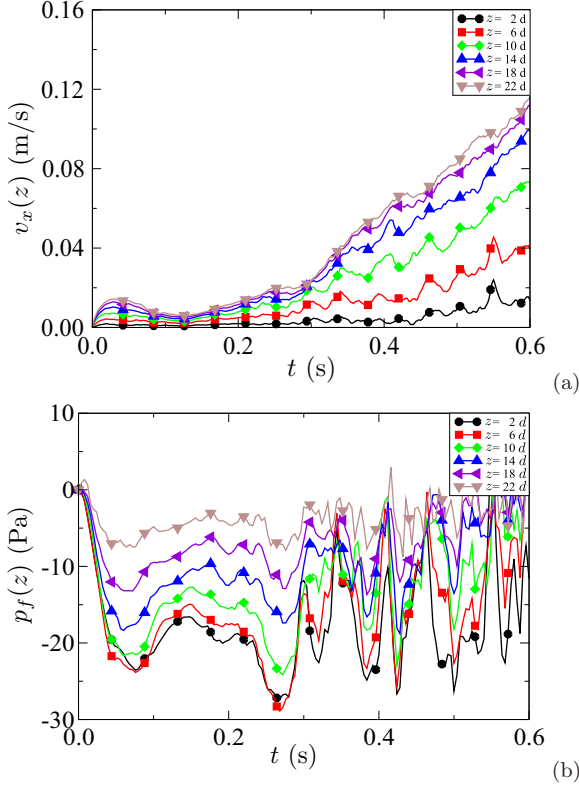


FIG. 10. (Color online) Velocity  $v_x(z)$  and fluid excess pressure  $p_f(z)$  as a function of time for different heights  $z$  and for packing fraction  $\nu_0 = 0.63$  and slope angle  $\theta = 26^\circ$ .

that remains nearly constant during creeping deformation at all heights with peak values slightly after tilting (reflecting the perturbation of the bed instantly rotated to a finite slope) and at failure (reflecting the instant loss of mechanical equilibrium).

The velocity profiles  $\langle v_x \rangle(z)$  and  $\langle v_z \rangle(z)$  obtained by time-averaging during creeping deformation are shown in Fig. 11 for three values of  $\theta$  and  $\nu_0 = 0.63$ . Apart from the lowermost layer, both components increase with height. The exact profiles cannot be determined accurately within our numerical precision. They are consistent with the Bagnold-type profile [38]. However, since the inertial numbers are rather low in the creeplike period, the velocity profile is expected to be linear. A change of slope seems to occur at  $z \simeq 15d$ . The low velocity gradient close to the free surface may be attributed to the drag force of the fluid above the bed. The bumpy bottom wall plays a similar role with respect to the lowermost layer. The time-averaged excess pressure  $\langle p_f \rangle(z)$  and dilatancy  $\langle \tan \psi \rangle(z)$  are displayed in Fig. 12. The excess pressure increases in absolute value almost quadratically with  $z$  from the free surface to the bottom and is well fitted by the predictions of the Darcy law, to be discussed in Sec. V. The dilatancy is rather high in the vicinity of the bottom wall but it declines and keeps a constant value  $\tan \psi \simeq 0.1$  for  $z > 7d$ , independent of  $\theta$ .

The above changes in the velocity and dilatancy profiles during the creeplike motion of the bed may reflect a partial shear localization inside the system due to the boundary effects at the top and bottom of the bed. This is the reason why in op-

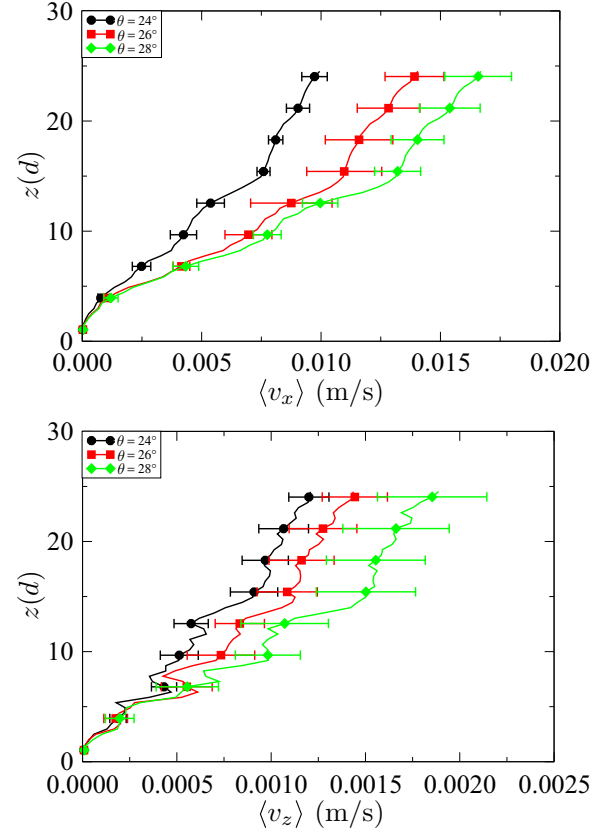


FIG. 11. (Color online) Velocity profiles  $\langle v_x \rangle(z)$  and  $\langle v_z \rangle(z)$  as a function of  $z$  and along the direction of the flow and perpendicular to the  $xy$  plane. The data are averaged over the creep period for each value of  $\theta$  and  $\nu_0 = 0.63$ . The error bars represent the corresponding standard deviations.

timizing the simulation cell with respect to the computational limits (numbers of grains and fluid nodes), a large aspect ratio  $H_s/L$  was preferred. Despite such irregularities and finite-size effects, all the data presented in this section and Sec. III are in good qualitative agreement with experiments.

## V. CONTINUUM MODEL

We expect from a continuum model of an immersed granular bed to provide a consistent description of the numerical observations presented in the last two sections. In particular, such a model should account for the stability of a dense bed inclined at an angle  $\theta$ , the time evolution of the packing fraction  $\nu$  and its value at failure, the triggering time  $t^{\text{trig}}$  as a function of the initial packing fraction  $\nu_0$  and  $\theta$ , and the failure criterion in terms of a well-defined value of the cumulative shear strain. Pailha *et al.* introduced a modified version of the poroelastic model of Iverson *et al.* together with an enhanced model of shear strength incorporating the effect of dilatancy to explain their experimental results [19,30]. The modeling approach presented in this section is based on very similar ingredients but formulated differently so as to separate the effects of dilatancy on the internal friction angle and excess pore pressure. We describe below the governing equations and then compare the predictions with our numerical data. We employ the usual sign

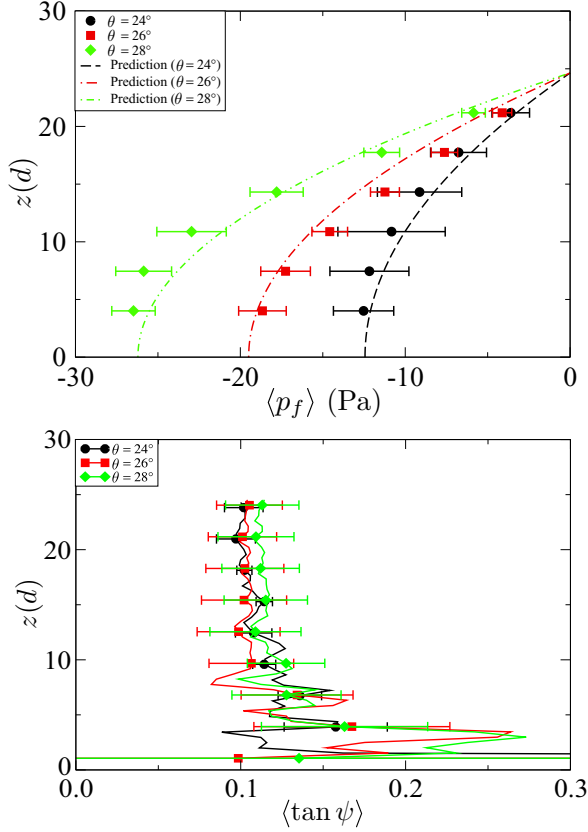


FIG. 12. (Color online) Excess pore pressure  $\langle p_f \rangle(z)$  and dilatancy  $\langle \tan \psi \rangle(z)$  averaged over time during creeplike for different slope angles  $\theta$  and for packing fraction  $\nu_0 = 0.63$ . The error bars represent the corresponding standard deviations. Dashed lines represent model predictions.

convention in granular materials with both stresses and strains counted as positive in compression.

### A. Stable and unstable states

According to the Mohr-Coulomb model, the stability of an inclined cohesionless granular bed is controlled by the internal friction coefficient  $\mu$ . The bed is stable for

$$\sigma'_{zx} \leq \mu \sigma'_{zz}, \quad (7)$$

where  $\sigma'_{zx}$  and  $\sigma'_{zz}$  are the stress components along and perpendicular to the bed. According to soil mechanics convention for grains immersed in a fluid, the “prime” denotes an “effective” stress supported by the grains. The total stress is the sum of stresses sustained by the fluid and grains and it is denoted without “prime.” The internal friction coefficient is a state-dependent property [40,41]. The steady shear flow of a granular material is characterized by the so-called “critical-state” friction coefficient  $\mu^*$ , which represents a material property in the quasistatic regime but increases with the inertial number  $I$ . The steady shear state is also characterized by a well-defined value of the packing fraction  $\nu^*$ , which decreases with  $I$ .

Depending on the loading conditions, the friction angle  $\mu$  can also become larger than  $\mu^*$  as a result of dilatancy. In a classical compression test, where the confining stress and

principal stress directions are imposed, starting with a dense and initially isotropic sample,  $\mu$  increases with shear strain towards a peak value  $\mu^+$  ( $> \mu^*$ ) before relaxing to the critical-state value  $\mu^*$  in steady shear. The peak friction coefficient  $\mu^+$  depends on the dilatancy angle  $\psi$  [15,22]. Assuming that elastic strain is negligible compared to plastic strain, such a relationship can be understood in terms of dissipation rates to which contribute both the shear stress and normal stress.

The dissipation rate due to shear stress is  $\dot{\epsilon}_{zx} \sigma'_{zx}$ . The normal stress  $\sigma_{zz}$  contributes only partially to dissipation since a fraction of the work supplied to the system is stored in the geometrical configuration, which expands against the normal stress. Hence, the dissipation rate due to normal stress is  $b \dot{\epsilon}_{zz} \sigma'_{zz}$ , where  $b$  is the dissipated fraction of the power supplied in the normal direction. We define an equivalent shear stress  $\sigma_{zx}^{\text{eq}}$  as the shear stress generating the same amount of dissipation without dilation,

$$W_{\text{dissip}} = \dot{\epsilon}_{zx} \sigma'_{zx} + b \dot{\epsilon}_{zz} \sigma'_{zz} \equiv \dot{\epsilon}_{zx} \sigma_{zx}^{\text{eq}}. \quad (8)$$

It is worth noting that the difference between  $W_{\text{dissip}}$  and the total input work  $W_{\text{in}} = \dot{\epsilon}_{zx} \sigma'_{zx} + \dot{\epsilon}_{zz} \sigma'_{zz} = (1 - b) \dot{\epsilon}_{zz} \sigma'_{zz}$  represents the reversible configurational energy that may be dissipated with delay if the configuration becomes unstable (e.g., at a stress peak state). We also define an equivalent internal friction angle  $\varphi^{\text{eq}}$  by setting

$$\tan \varphi^{\text{eq}} = \frac{\sigma_{zx}^{\text{eq}}}{\sigma'_{zz}}, \quad (9)$$

whereas the current friction angle  $\varphi$  of the granular material is given by

$$\tan \varphi = \frac{\sigma'_{zx}}{\sigma'_{zz}}. \quad (10)$$

With these definitions, Eq. (8) becomes

$$\tan \varphi = \tan \varphi^{\text{eq}} + b \tan \psi. \quad (11)$$

Equation (11) should simply be considered as a definition of the equivalent friction angle  $\varphi^{\text{eq}}$ . Note, however, that this equation implies that  $\varphi^{\text{eq}}$  in steady shear, where  $\psi = 0$  equals the critical-state friction angle  $\varphi^*$ . This provides thus a physical interpretation of  $\varphi^{\text{eq}}$  as an intrinsic parameter that, as postulated by Taylor [42], determines the dissipation rate irrespective of the mechanical state of the material. On the other hand, the maximum value  $\varphi^+$  of the internal friction angle occurs for the peak dilatancy  $\psi^+$ , which happens at the beginning of the creeplike phase as the granular bed is inclined above its angle of repose. Hence, by setting  $\varphi^{\text{eq}} = \varphi^*$ , we get

$$\tan \varphi^+ = \tan \varphi^* + b \tan \psi^+. \quad (12)$$

In a linear approximation,  $\psi^+$  may be estimated from the difference between the initial packing fraction  $\nu_0$  and the critical packing fraction  $\nu^*$ , which corresponds to zero dilatancy [19,22,40],

$$\tan \psi^+ = a(\nu_0 - \nu^*). \quad (13)$$

Experimental measurements yield  $a \simeq 3$ . We can directly check this relation from our data. Figure 13 shows the maximum dilatancy  $\tan \psi^+$  at the beginning of the creeplike phase as a function of  $\nu_0$  for all our simulations in the dense

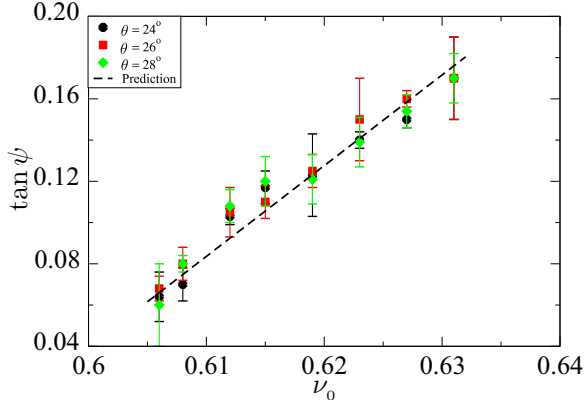


FIG. 13. (Color online) Maximum dilatancy as a function of the initial packing fraction for all our data in the creep regime. The dotted line represents a linear regression of slope  $\simeq 4.4$ .

regime. Up to fluctuations, we observe a nearly linear relation with  $a \simeq 4.4$  and  $\nu^* \simeq 0.59$ . The value of  $a$  is expected to reflect the nature of the granular material (e.g., size distribution and particle shapes).

Combining Eqs. (12) and (13), we get the peak friction coefficient as a function of the initial packing fraction,

$$\mu^+ = \mu^* + ab(\nu_0 - \nu^*). \quad (14)$$

A tilted granular bed is stable for  $\theta \leq \theta^+ = \varphi^+$  and unstable otherwise. But upon flow,  $\varphi$  declines from  $\varphi^+$  to  $\varphi^*$ . We shall see below that the parameter  $b$  may be evaluated from the data, yielding  $b \simeq 0$  so in our system no dissipation occurs by dilation during the creeplike period and thus the critical slope is  $\theta^+ \simeq \varphi^*$ .

### B. Stabilization by negative excess pore pressure

A dry bed inclined at an angle  $\theta > \varphi^+$  is unstable. But when immersed in a fluid, it can be stabilized as a result of the buildup of a negative excess pressure  $p_f(z)$  ( $< 0$ ) of the fluid induced by bed dilation. The effect of the negative excess pressure in the pore space is to enhance the normal stress inside the packing so the vertical load becomes

$$\sigma'_{zz}(z) = \sigma_{zz}^h(z) - p_f(z), \quad (15)$$

where  $\sigma_{zz}^h(z)$  is the vertical hydrostatic stress given by the relative weight of the grains,

$$\sigma_{zz}^h(z) = \nu g(\rho_s - \rho_f)(H_s - z) \cos \theta. \quad (16)$$

Hence, the bed is stabilized by the fluid if

$$\sigma'_{zx}(z) \leq \mu^+ [\sigma'_{zz}(z) - p_f(z)]. \quad (17)$$

This condition can be expressed as

$$\tan \theta = \frac{\sigma'_{zx}(z)}{\sigma'_{zz}(z)} \leq \mu^+ \left\{ 1 - \frac{p_f(z)}{\sigma_{zz}^h(z)} \right\}. \quad (18)$$

This inequality describes a cohesive-like bed with  $p_f(z)/\sigma_{zz}^h(z)$  representing the relative cohesion of the material. Since the bed is unstable in the absence of the fluid, the pore pressure is mobilized just as much as to restore equilibrium. The angle  $\theta$  being imposed, the above inequality becomes an equation

only for a particular value of  $z$  where  $p_f(z)/\sigma_{zz}^h(z)$  takes its lowest value.

The excess pressure  $p_f(z)$  is a consequence of the normal dilation of the bed. According to Darcy's law,

$$v_z^{sf}(z) = -\frac{k}{\eta} \frac{dp_f}{dz}, \quad (19)$$

where  $v_z^{sf}(z)$  is the ‘‘superficial’’ fluid velocity with respect to the granular skeleton at height  $z$  and

$$k = \frac{1}{c} \frac{(1-\nu)^3}{\nu^2} d^2 \quad (20)$$

with the Kozeny-Carman coefficient  $c \simeq 150$ . The mass conservation of incompressible fluid implies that the pore fluid flow rate (i.e., superficial fluid velocity) in the  $z$  direction at height  $z$  should be equal and opposite to the  $z$ -direction velocity  $v_z^s(z)$  of the granular skeleton at height  $z$ ,

$$v_z^{sf} = -v_z^s. \quad (21)$$

Hence, assuming that the normal strain rate  $\dot{\epsilon}_{zz} = v_z^s(z)/z$  is homogeneous, we have

$$\frac{dp_f}{dz} = -\frac{c}{d^2} \eta \frac{\nu^2}{(1-\nu)^3} z \dot{\epsilon}_{zz}. \quad (22)$$

This equation may be integrated across the bed with the boundary condition of  $p_f(z = H_s) = 0$ . This yields

$$p_f(z) = \frac{c}{2d^2} \eta \frac{\nu^2}{(1-\nu)^3} (H_s^2 - z^2) \dot{\epsilon}_{zz}. \quad (23)$$

The half-quadratic profile of the excess pressure predicted by Eq. (23) is in good agreement with the data without adjusting parameters as shown in Fig. 12.

As a result of periodic boundary conditions along  $x$  and  $y$  directions, the normal strain rate of the bed is related to the rate of change of the packing fraction,

$$\dot{\epsilon}_{zz} = \frac{\dot{\nu}}{\nu}. \quad (24)$$

From Eqs. (16), (23), and (24), we finally get the following expression for the relative cohesion induced by the fluid:

$$\frac{p_f(z)}{\sigma_{zz}^h(z)} = \frac{c}{2d^2} \eta \frac{1}{(1-\nu)^3} \frac{1}{(\rho_s - \rho_f)g \cos \theta} (H_s + z) \dot{\nu}. \quad (25)$$

This equation shows that the excess pore pressure contribution depends on the current value  $\nu$  of the packing fraction and inclination angle  $\theta$  of the bed (within the range considered here). It increases linearly in absolute value with the height  $z$  so its lowest level occurs at the bottom of the bed. This means that if the condition of mechanical equilibrium (18) is fulfilled at the bottom as an equation (replacing the inequality), then it will be satisfied everywhere else inside the bed as an inequality. Let us set

$$R = 1 - \frac{p_f(z=0)}{\sigma_{zz}^h(z=0)}. \quad (26)$$

From Eq. (18), the condition of equilibrium at the bottom of the bed thus can be expressed as

$$\tan \theta = \mu^+ \left\{ 1 - \frac{p_f(z=0)}{\sigma_{zz}^h(z=0)} \right\} = \mu^+ R. \quad (27)$$

Given the expression of  $\mu^+$  in (14), the condition of equilibrium takes finally the following form:

$$R = \frac{\tan \theta}{\mu^* + ab(\nu_0 - \nu^*)} \quad (28)$$

and the evolution of packing fraction is governed by

$$\frac{\dot{\nu}}{\nu_0} = -\frac{(1-\nu)^3}{(1-\nu_0)^3} \frac{1}{t_c} \quad (29)$$

with the characteristic time

$$t_c = c \frac{\eta H_s}{2d^2 (\rho_s - \rho_f) g \cos \theta} \frac{1}{(1-\nu_0)^3} \frac{\nu_0}{R-1}. \quad (30)$$

Equation (28) indicates that  $R$  is a function only of the slope  $\theta$  and the initial packing fraction and thus, for a given value of  $\theta$  and  $\nu_0$ , it remains constant during creeplike deformation until slope failure. This implies that the pore pressure is constant during creep, in agreement with our simulation data shown in Fig. 10 disregarding the initial peak value due to sudden inclination of the bed. Relying on Eq. (28), we may obtain the value of the parameter  $b$  by plotting  $\tan \theta / \langle R \rangle$  as a function of  $\nu_0$ , as shown in Fig. 14. We see that the data points for different slopes are independent of  $\nu_0$ , which means that the parameter  $b$  in equation (28) is almost zero within our data precision. This is in agreement with experimental data of Pailha *et al.* [19] as well as the classical theoretical development of work equation by Taylor [42] and Schofield and Wroth [14]. Interestingly, we observe instead that the ratio  $\tan \theta / \langle R \rangle$  increases with  $\theta$ . With  $b = 0$  in Eq. (28), this implies that  $\mu^*$  varies with  $\theta$ . This is an unexpected behavior since  $\mu^*$  is in principle an intrinsic property of the granular material. We will propose in Sec. VI an interpretation of this behavior in terms of enhanced structural anisotropy in a granular system stabilized above its angle of repose.

Since  $R$  is constant, the characteristic time  $t_c$  is also a constant of the creeplike flow. Hence, Eq. (29) can be solved exactly to yield

$$\nu(t) = 1 - (1 - \nu_0) \left\{ 1 - \frac{2\nu_0}{1 - \nu_0} \frac{t}{t_c} \right\}^{-1/2}. \quad (31)$$

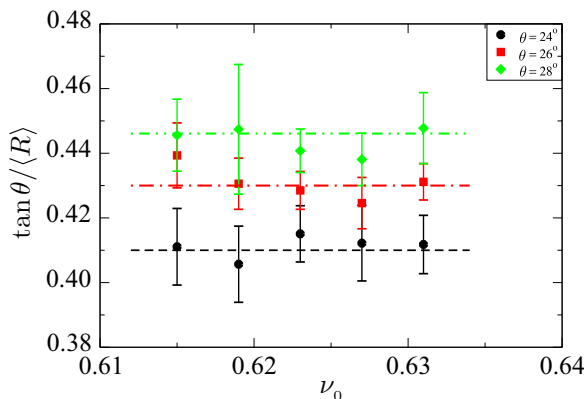


FIG. 14. (Color online)  $\tan \theta / \langle R \rangle$  as a function of initial packing fraction  $\nu_0$  for three values of the slope angle  $\theta$ . The dashed lines represent the mean level for each value of  $\theta$ .

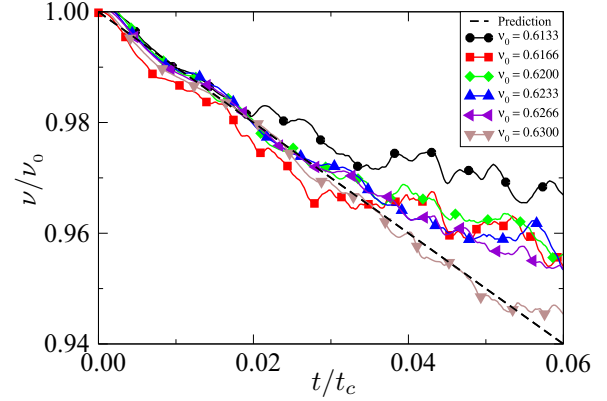


FIG. 15. (Color online) Normalized packing fraction  $\nu/\nu_0$  as a function of time normalized by the characteristic time  $t_c$  for different values of  $\nu_0$  and  $\theta = 26^\circ$ . The dotted line of slope  $-1$  is the predicted scaling.

In the limit  $t \ll t_c$ , which is the case for creep where the triggering time  $t^{\text{trig}}$  is quite small compared to  $t_c$ , and at leading order in  $t$ , we have

$$\frac{\nu(t)}{\nu_0} \simeq 1 - \frac{t}{t_c}. \quad (32)$$

This equation fits excellently the observed linear decrease of the packing fraction  $\nu$  with time as shown in Fig. 5. It suggests furthermore that all the data should collapse during the creeplike period by simply normalizing  $t$  by the characteristic time  $t_c$  and  $\nu$  by  $\nu_0$ . This scaling works excellently, as shown in Fig. 15, for all our simulation data with different values of  $\nu_0$  and  $\theta$ . For different values of  $\nu_0$ , we see that the packing fraction follows closely the straight line of slope  $-1$  during creeplike motion and deviates from the line only when the slope fails.

Equation (31) also implies that the normal strain rate is nearly constant during the creep period due to interaction of pore fluid flow and dilation rate of the material,

$$\dot{\varepsilon}_{zz} = \frac{\dot{\nu}}{\nu} \simeq \frac{\dot{\nu}}{\nu_0}. \quad (33)$$

As a result, the cumulative normal strain is a linear function of time,

$$\varepsilon_{zz}(t) \simeq -\frac{t}{t_c}. \quad (34)$$

Figure 16 shows  $\varepsilon_{zz}$  as a function of normalized time for different values of  $\nu_0$  and  $\theta$ . We see that all data points collapse on a straight line of slope 1 as predicted by Eq. (34).

### C. Slope failure

The mechanism of slope stabilization by dilation  $\dot{\varepsilon}_{zz}$  inside a fluid contains also the germ of slope failure as a result of the linear decrease of packing fraction. It is important to note that the evolution of  $\nu$  occurs under constant stress and, hence, it does not change the structure of governing equations during creep as described previously. This means that, although the evolution of  $\nu$  can be deduced from those equations, its triggering value and the triggering time can

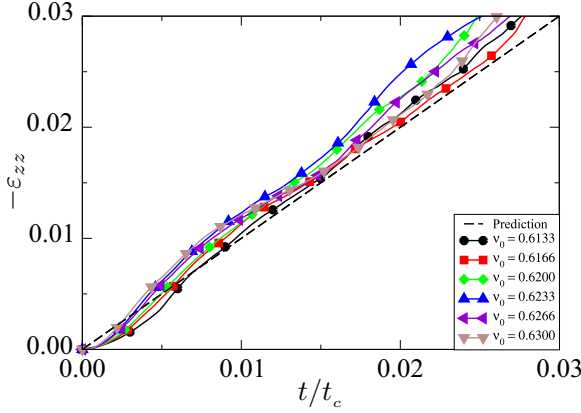


FIG. 16. (Color online) Cumulative strain along  $z$  as a function of the normalized time for different values of  $\nu_0$  and for  $\theta = 26^\circ$ . The dashed line of slope 1 is predicted by the model.

not be predicted. The slope failure occurs as a discontinuous transition that is triggered when the packing fraction cannot keep dilating without losing its force-bearing structure. The problem is that, as it was seen previously, the packing fraction  $\nu^{\text{trig}}$  at failure is larger than the steady-state packing fraction  $\nu^*$ , and it depends on the initial packing fraction  $\nu_0$ . Hence, there is no intrinsic value of the packing fraction defining a criterion of failure.

In a similar vein, the cumulative normal strain at failure  $\varepsilon_{zz}^{\text{trig}}$  increases linearly with  $\nu_0$ , and for this reason it does not represent a good candidate as failure criterion. In contrast, according to the simulation data, the cumulative shear strain at failure is  $\varepsilon_{zx}^{\text{trig}} \simeq 0.2$ , almost independent of both  $\nu_0$  and  $\theta$ . This value is quite close to the experimental result and may be used in combination with Eqs. (34) and (13) to predict the triggering time. We get

$$\frac{t^{\text{trig}}}{t_c} \simeq a(\nu_0 - \nu^*) \varepsilon_{zx}^{\text{trig}}. \quad (35)$$

This equation shows that  $t^{\text{trig}}$  scales with  $t_c$ . For typical values of  $\nu_0$  and  $\nu^*$ , the ratio  $t^{\text{trig}}/t_c$  is small, justifying thus *a posteriori* the linear approximation of Eq. (31), which led to Eq. (32). To check the relation (35), we have plotted in Fig. 17  $t^{\text{trig}}/t_c$  as a function of  $\nu_0$  for  $\varepsilon_{zx}^{\text{trig}} = 0.2$  and  $\nu^* = 0.59$ . Here again, up to fluctuations, we obtain data collapse on a straight line of slope  $a\varepsilon_{zx}^{\text{trig}} \simeq 4.4 \times 0.2 = 0.88$ .

It should be noted here that part of the dependence of  $t^{\text{trig}}$  on  $\nu_0$  is hidden in  $t_c$ . The full dependence can be obtained from Eqs. (35) and (30) as follows:

$$t^{\text{trig}} \propto \nu_0^2 (\nu_0 - \nu^*) / (1 - \nu_0)^3. \quad (36)$$

This is the prediction that was plotted in Fig. 8, and which fits well our data with a numerical factor that depends only on  $\theta$ .

Inserting the expression of  $t^{\text{trig}}$  in Eq. (32), we also get the value of packing fraction at failure,

$$\nu^{\text{trig}} \simeq \nu_0 \left\{ 1 - a(\nu_0 - \nu^*) \varepsilon_{zx}^{\text{trig}} \right\}. \quad (37)$$

This equation yields an intermediate value between  $\nu_0$  and  $\nu^*$ . The predicted values of  $\nu^{\text{trig}}$  are in good agreement with our data for  $a = 4.4$  and  $\varepsilon_{zx}^{\text{trig}} = 0.2$ , as shown in Fig. 8. This

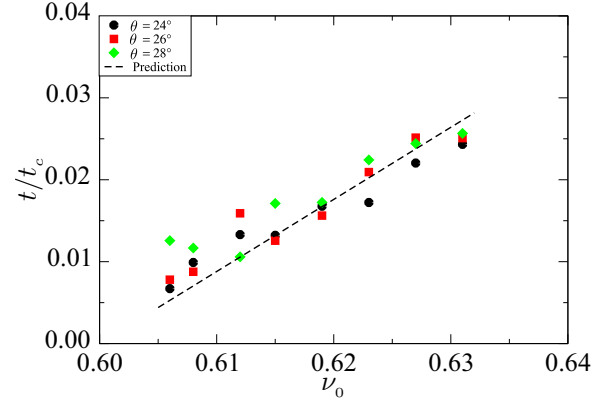


FIG. 17. (Color online) Normalized triggering time  $t^{\text{trig}}/t_c$  as a function of  $\nu_0$  for different values of  $\theta$ . The dashed straight line of slope 0.88 represents the model prediction.

equation indicates that  $\nu^{\text{trig}}$  tends to zero as  $\nu_0$  approaches  $\nu^*$ . However, for  $\nu_0 < 0.6$ , the difference  $\nu^{\text{trig}} - \nu_0$  is at most 0.005. This difference is too small to be discerned within numerical or natural physical fluctuations of the system, so in such limits  $\nu^{\text{trig}} \simeq \nu_0$ , i.e., the slope fails without creep instantaneously.

## VI. EVOLUTION OF THE CONTACT NETWORK

In this section, we investigate the evolution of the internal structure of the granular bed during creeplike deformation. One issue is whether the slope failure at  $\varepsilon_{zx}^{\text{trig}} \simeq 0.2$  can be understood from the evolution of the contact network and force chains. Another issue is the dependence of  $\mu^*$  on  $\theta$ .

The contact network can be described by its connectivity and anisotropy. At the lowest order, the connectivity is characterized by the mean coordination number  $Z$  for force-transmitting contacts. The anisotropy at the lowest order is characterized by the fabric tensor  $F_{\alpha\beta}$  defined from the contact normals  $\vec{n}$  [38,41,43–45],

$$F_{\alpha\beta} = \langle n_\alpha n_\beta \rangle, \quad (38)$$

where the average runs over the set of force-transmitting contacts inside the bed. By definition,  $\mathbf{F}$  is symmetric and  $\text{tr}(\mathbf{F}) = \mathbf{1}$ . Due to periodic boundaries along  $y$ , we consider the restriction of  $\mathbf{F}$  to the  $xz$  plane with principal values  $F_1$  and  $F_3$ . The anisotropy of the network in the plane is defined as follows:

$$a_c = 2 \frac{F_1 - F_3}{F_1 + F_3}. \quad (39)$$

The factor 2 in this definition is mandatory and is introduced by analogy with the Fourier expansion of the probability distribution  $P(\vec{n})$  of contact orientations  $\vec{n}$  [46]. The major principal direction  $\theta_c$  of the fabric tensor in the  $xz$  plane represents the privileged contact direction.

Figure 18 shows the evolution of  $Z$  and  $a_c$  for several values of  $\nu_0$  in the dense cases as a function of the cumulative shear strain  $\varepsilon_{zx}$ . The initial value of  $Z$  after tilting is  $\simeq 4.7$  but is slightly higher for larger  $\nu_0$ . Remarkably,  $Z$  keeps a nearly constant level during the creeplike period and begins to decline only after failure at  $\varepsilon_{zx} = 0.2$ . This is quite unexpected

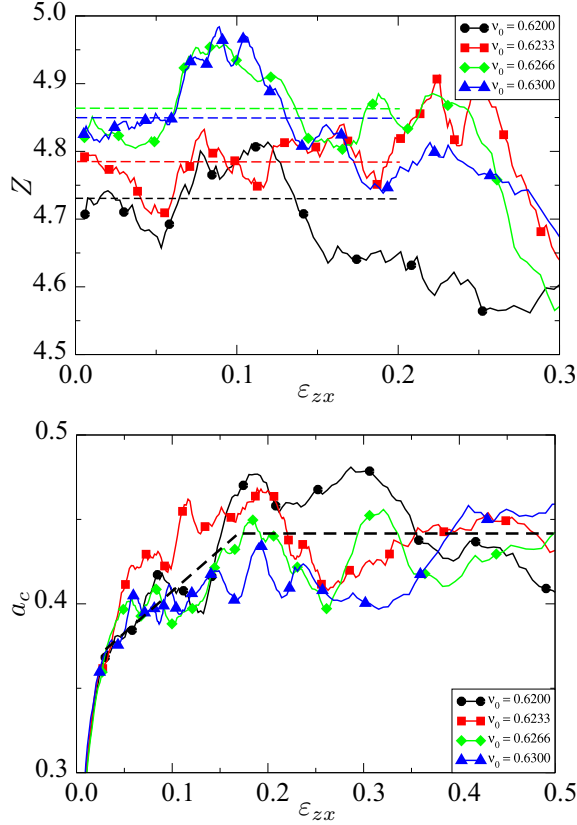


FIG. 18. (Color online) Coordination number  $Z$  and contact anisotropy  $a_c$  for several values of  $\nu_0$  and for  $\theta = 26^\circ$  in the dense regime as a function of the cumulative shear strain  $\varepsilon_{zx}$ . The dashed lines are guides to the eyes, indicating the nearly constant mean of  $Z$  until slope failure at  $\varepsilon_{zx} \simeq 0.2$  for each value of  $\nu_0$  and the increase of the anisotropy at the same time and its nearly constant value after failure.

since the bed flows and dilates and, as the grains are tightly packed in the dense regime, one expects more contact loss than contact gain during this period. This behavior may be attributed to the negative excess pore pressure and lubrication forces that both work to prevent the contacts from opening. It is also interesting that the anisotropy  $a_c$  increases considerably from  $\simeq 0.35$  and levels off at a constant value  $a_c^{\text{trig}} \simeq 0.45$  at  $\varepsilon_{zx} \simeq 0.2$ . It is generally observed that the anisotropy evolves mainly by contact gain along the direction of contraction  $\theta_\varepsilon$  and contact loss along the direction of expansion  $\theta_\varepsilon + \pi/2$ . But since  $Z$  is nearly constant during the creep-like period, the only possible mechanism for the evolution of  $a_c$  in our system is the distortion of the contact work. In contrast, after failure,  $Z$  declines and therefore the constant value of  $a_c$  reflects the balance between contact loss and gain along the directions of extension and contraction, respectively.

Figure 19 shows the evolution of the privileged contact direction  $\theta_c$  and the major principal stress direction  $\theta_\sigma$  as a function of  $\varepsilon_{zx}$ . For all values of  $\nu_0$ , the privileged contact direction  $\theta_c$  is vertical before tilting due to the preparation procedure, but it declines rapidly down to nearly  $42^\circ$  after tilting and then rotates slowly towards  $45^\circ$  at failure. We observe the same trends for  $\theta_\sigma$ .

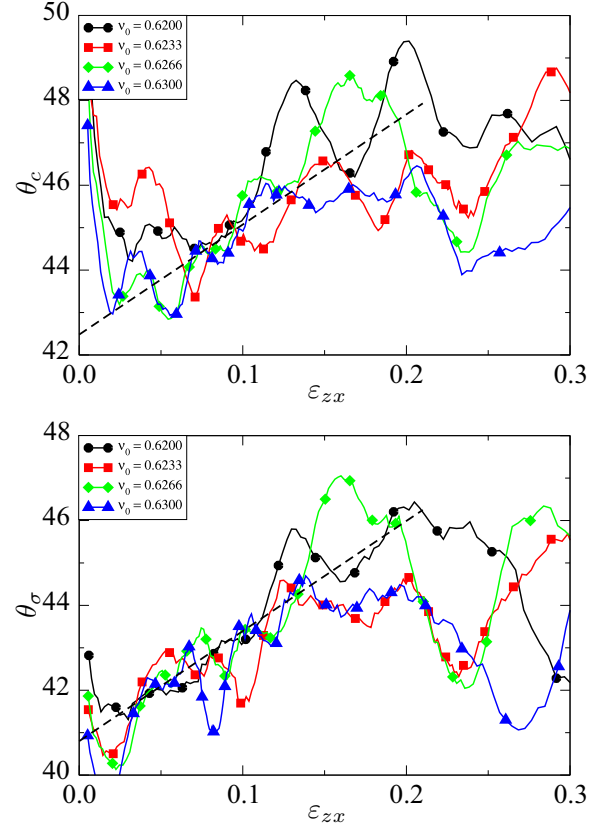


FIG. 19. (Color online) Evolution of the privileged contact direction  $\theta_c$  and the major principal stress direction  $\theta_\sigma$  as a function of  $\varepsilon_{zx}$  for several values of  $\nu_0$  and for  $\theta = 26^\circ$ . The dashed lines indicate the linear trend.

The reorientation of the contacts and stresses during tilting is due to contact gain and loss. The shear direction being imposed by the boundary conditions, the direction of contraction with respect to the flow direction  $x$  is given by  $\theta_\varepsilon = \pi/4 - \psi/2$  [47]. With  $\psi \simeq \tan^{-1}(0.1)$ , we get  $\theta_\varepsilon \simeq 42^\circ$ , in agreement with the simulation data. The subsequent rotation towards  $45^\circ$  during the creep-like period at constant  $Z$  occurs mainly by distortion of the contact network.

The above description should be contrasted with the usual Mohr-Coulomb analysis, which implies  $\theta_\sigma = \pi/4 - \varphi/2$  [47]. In fact, this criterion is based on the assumption that the shear strength is isotropic or that the fabric is sufficiently mobilized to reach a reference state, such as the “critical state” or the stress peak state, in the direction of deformation. In our system, the inclination of the bed corresponds to the rotation of the fabric with respect to the gravity forces acting on the grains and the mobilization of excess pore pressure to ensure stability for an angle above the angle of repose. This is not a common equilibrium state and, hence, the stress direction is controlled by the evolution of the contact network rather than external forces acting on the system. As the contact network deforms with a characteristic time set by the viscous forces acting between grains, the bed tends to an unstable state where the distortion can no more continue without volume change. But even a tiny contraction of the system at such a marginal state of stability is amplified by the lubrication forces, leading to

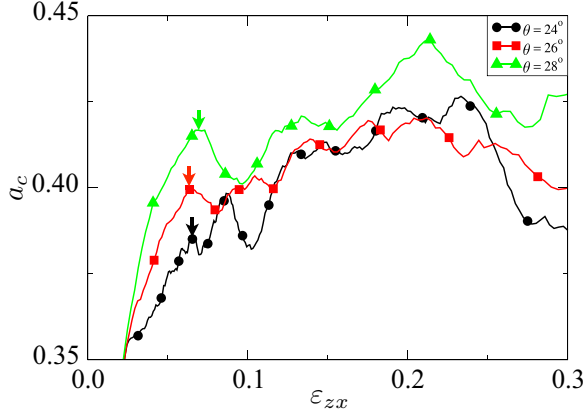


FIG. 20. (Color online) Contact anisotropy as a function of the cumulative shear strain  $\varepsilon_{zx}$  for three values of inclination angle  $\theta$  and  $\nu_0 = 0.63$ . The arrows indicate the initial anisotropies shortly after tilting.

irreversible failure of the slope. This bifurcation is similar to liquefaction except that it is triggered by the distortion of the microstructure with respect to the gravity rather than the evolution of stresses. At failure, the grain-fluid mixture has the features of a liquid with the stress and strain-rate directions both orientated at  $\pi/4$  with respect to flow direction.

Another feature that we would like to analyze in terms of the structural anisotropy is the increase of  $\mu^*$  with  $\theta$ . In a geometrical interpretation of the critical state,  $\mu^*$  reflects the structure of the contact network, described by  $Z$  and  $a_c$ . It is well known that the internal friction is a linear function of  $a_c$  [41,43,46,48,49]. Figure 20 shows the evolution of  $a_c$  for three inclination angles as a function of cumulative shear strain. We see that  $a_c$  is an increasing function of  $\theta$ , implying that the internal friction is also a function of  $\theta$ . In particular, its first peak value  $a_{c0}$  just after inclination, marked by an arrow in Fig. 20, increases linearly with  $\theta$ . This increase of  $a_{c0}$  is a natural consequence of the rotation of the granular bed beyond its angle of repose  $\theta_r$ . In other words, it reflects the fact that the slope is stabilized by a negative pore pressure, which acts as an effective cohesion-like parameter. This cohesion induces thus an extra anisotropy that may be approximated as depending linearly on  $\tan \theta$  [48],

$$\Delta a_{c0} = a_{c0}(\theta) - a_{c0}(\theta_r) \propto (\tan \theta - \tan \theta_r). \quad (40)$$

We now assume that  $\mu^*$  is a linear function of  $\Delta a_{c0}$ , as discussed above. Hence,

$$\mu^*(\theta) = \mu^*(\theta_r) + s(\tan \theta - \tan \theta_r), \quad (41)$$

where  $s$  is a constant depending only on the material. Given that  $\mu^*(\theta_r) = \tan \theta_r \simeq 0.4$  in our system, the data points of Fig. 14 are consistent with Eq. (41) for  $s \simeq 0.3$ .

From Eqs. (14) and (41), we finally get the following expression for  $R$  as a function of  $\theta$ :

$$R = \frac{\tan \theta}{\tan \theta_r} \frac{1}{1 + s \left( \frac{\tan \theta}{\tan \theta_r} - 1 \right)}. \quad (42)$$

This is an interesting relation as it makes depend  $R$  only on  $\theta$ , so its validity goes beyond the effect of fluid and covers slope stabilization by cohesion in general. It correctly predicts the

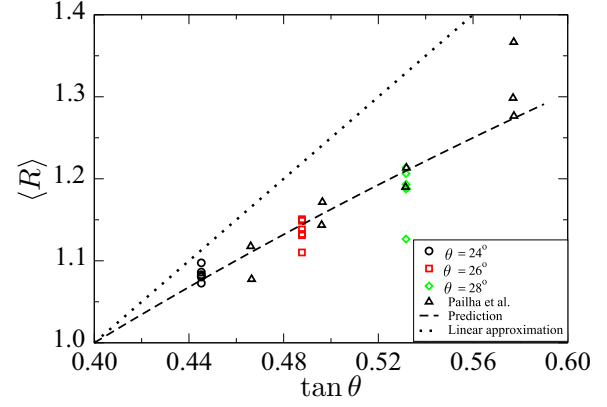


FIG. 21. (Color online) The mean value of  $R$  during creep deformation as a function of inclination angle  $\theta$ . The simulation data are given for  $24^\circ$ ,  $26^\circ$ , and  $28^\circ$  and several values of the packing fraction. The experimental data extracted from Ref. [19] are also shown. The dashed line shows the proposed fitting form, whereas the dotted line represents the linear approximation  $\langle R \rangle = \tan \theta / \tan \theta_r$  with  $\theta_r = 22^\circ$ .

value  $R = 1$  for  $\theta = \theta_r$ . In this limit, the slope is stable and the excess fluid pressure is not mobilized. Figure 21 shows  $\langle R \rangle$  as a function of  $\tan \theta$  with all our simulations data for the three angles  $24^\circ$ ,  $26^\circ$ , and  $28^\circ$  and different packing fractions, together with data points extracted from the experiments of Pailha *et al.* [19]. We see that Eq. (42) with  $s = 0.3$  and  $\theta_r = 22^\circ$  correctly fits all the data, both numerical and experimental. The curvature of this fitting form is a crucial parameters since a linear approximation (with  $s = 0$  but with  $\theta_r = 22^\circ$ ), shown also in Fig. 21, considerably overestimates the data.

In summary, the creeplike deformation of the packing stabilized by negative excess pore pressure is governed by a novel mechanism, namely the distortion of the contact network at constant coordination number. The inclined bed is destabilized when this mechanism is exhausted: the contact anisotropy levels out and dilatancy vanishes instantly at a packing fraction above the critical packing fraction. After failure, the contact network can deform by the more common mechanism of loss and gain of contacts. The extra anisotropy induced by tilting the bed above its angle of repose suggests also a physically plausible description of the linear dependence of the internal friction angle on the inclination angle, and therefore a nonlinear dependence of the excess pore pressure on the inclination angle. This also shows that the ambient fluid affects the behavior both directly through the negative excess pore pressure induced by dilatancy, with its stabilizing effect on the bed, and indirectly by allowing the bed to develop an extra anisotropy of the contact network, which tends to stabilize the bed by increasing its internal friction.

## VII. CONCLUSION

In this paper, we used a 3D-coupled DEM-LBM algorithm with appropriate boundary conditions to investigate the spatiotemporal process of the initiation of slope failure in a granular bed of rigid grains immersed in a viscous fluid. Our simulation data were shown to be in qualitative and quantitative

agreement with the available experimental results despite the low number of grains in the simulations imposed by the large number of fluid degrees of freedom in the pore space. We analyzed in detail the evolution of macroscopic observables such as shear strain, packing fraction, and excess pore pressure for different values of the initial packing fraction and slope angle. Two regimes were evidenced as in experiments: a loose regime where the slope fails spontaneously and a dense regime where the failure is delayed by a negative excess pressure built up in reaction to the dilation of the bed. As in experiments, the two regimes belong to the packing fractions below and above 0.59, respectively.

We focused in more detail on the creeplike deformation of the inclined bed in the dense regime. The time evolutions of the packing fraction and shear strain were shown to scale with a characteristic time extracted from a model based on the balance of granular stresses in the presence of a pore excess pressure and the relation of the latter with dilatancy rate controlled by Darcian drag forces. The cumulative shear strain at failure was found to be around 0.2, close to the experimental value, irrespective of the initial packing fraction and inclination angle. In the same way, the time and packing fraction at slope failure were found to be correctly predicted by the model.

We also analyzed the evolution of the contact network during the creeplike period. A remarkable finding is that the network deforms by distortion at a nearly constant connectivity. The contact network anisotropy grows with shear strain, and slope failure is triggered when the anisotropy saturates. The anisotropy appears thus as an internal variable, reflecting the distortion of the contact network. The independence of the internal friction angle with respect to the initial packing fraction and its dependence on the slope angle were discussed and argued to be a consequence of slope stabilization by the cohesive-like effect of negative excess pore pressure. It is also interesting to note that the transition from stable equilibrium to inertial flow in the presence of a fluid is accompanied by large fluctuations. As soon as the capacity of volume change by distortion is nearly exhausted, the slope instability is triggered by these fluctuations and amplified by lubrication forces as the avalanches proceeds.

We believe that the postfailure dynamics and the nature of fluctuations during the avalanching transient merit a dedicated investigation. We are also interested in the steady-state flow that is reached after the transient. In this paper, we addressed neither the role of fluid viscosity nor the relative density of grains with respect to fluid, which control the relative effects of fluid and grain inertia. A systematic investigation of different flow regimes is currently underway, and the results will be reported in a future paper. This work clearly demonstrates the interest and feasibility of numerical simulations of immersed granular materials in relation to both experiments and theoretical models with the advantage of providing direct access to the grain-scale variables and microstructure.

## APPENDIX A: COUPLED LBM-DEM METHOD

We present here a brief description of the LBM as a time-stepping scheme for the numerical integration of Navier-Stokes equations governing fluid motion and its coupling

with the molecular dynamics-type DEM for the integration of Newton's equations of motion for rigid particles interacting via frictional contacts in 3D. We discuss the discretization approach for fluid-particle interactions and necessary precautions in the choice of parameters.

### 1. Lattice Boltzmann Method (LBM)

The LBM is based on a material representation of fluids as consisting of particles moving and colliding on a lattice [50–53]. Partial distribution functions  $f_i(\vec{r}, t)$  are introduced to represent the probability density of a particle at the position  $\vec{r}$  at time  $t$  with a velocity  $\vec{v} = \vec{c}_i$  along discrete direction  $i$ . Figure 22 shows the meshing scheme D3Q19, corresponding to 18 space directions in 3D, which we used in our simulations. The distribution functions evolve at each node according to a set of rules, which are constructed to ensure the conservation equations of mass, momentum, and energy and thus to recover the incompressible Navier-Stokes equations [54]. This holds only when the wave lengths are small compared to the lattice spacing unit [55].

At each node, the fluid density  $\rho$  and velocity  $\vec{u}$  are defined as

$$\rho = \sum_i f_i, \quad (\text{A1})$$

$$\rho \vec{u} = \sum_i f_i \vec{c}_i. \quad (\text{A2})$$

and the temperature is given by

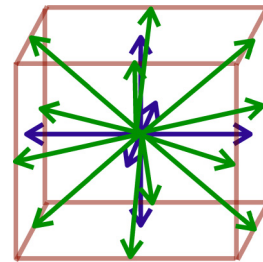
$$\frac{D}{2} kT = \sum_i \frac{1}{2} m (\vec{c}_i - \vec{u})^2 \frac{f_i}{\rho}, \quad (\text{A3})$$

where  $m$  is particle mass and  $k$  is the Boltzmann constant. The equilibrium state is assumed to be governed by the Maxwell distribution as follows:

$$f^{\text{eq}}(\vec{c}) = \rho \left( \frac{m}{2\pi kT} \right)^{3/2} \exp \left( -\frac{m}{2kT} (\vec{c} - \vec{u})^2 \right), \quad (\text{A4})$$

where  $\vec{u}$  is the mean velocity. By expanding (A4) to order 2 as a function of  $u/c_s$ , which is the local Mach number with  $c_s$  being the sound velocity, a discretized form of the Maxwell distribution is obtained and used in the LBM,

$$f^{\text{eq}} = \rho w_i \left( 1 + b \frac{\vec{c}_i \cdot \vec{u}}{c_s^2} + e \frac{u^2}{c_s^2} + h \frac{(\vec{c}_i \cdot \vec{u})^2}{c_s^4} \right), \quad (\text{A5})$$



D3Q19

FIG. 22. (Color online) A 3D LBM scheme.



where the factor  $w_i$  and the coefficients  $b$ ,  $e$ , and  $h$  depend on the scheme with the requirement of rotational invariance [56]. The sound speed is then given by  $c_s = \sum_i w_i c_i^2$ . For the D3Q19 scheme, we have  $c_s = c/\sqrt{3}$ , where  $c = \delta x/\delta t_{\text{LBM}}$  is the lattice velocity defined as the ratio of the basic lattice spacing  $\delta x$  to the LBM time step  $\delta t_{\text{LBM}}$  and  $c_s^2 = RT$ .

The velocities evolve according to the Boltzmann equation. In its discretized form, it requires an explicit expression of the collision term. We used the Bhatnagar-Gross-Krook (BGK) model in which the collision term for each direction  $i$  is simply proportional to the distance from the Maxwell distribution [57],

$$\frac{\partial f_i}{\partial t_{\text{coll}}} = \frac{1}{\tau} [f_i^{\text{eq}}(\vec{r}, t) - f_i(\vec{r}, t)], \quad (\text{A6})$$

where  $\tau$  is a characteristic time. Hence, for the D3Q19 scheme, we have a system of 18 discrete equations governing the distribution functions,

$$f_i(\vec{r} + \vec{c}_i \delta t, t + \delta t) = f_i(\vec{r}, t) + \frac{1}{\tau} [f_i^{\text{eq}}(\vec{x}, t) - f_i(\vec{r}, t)]. \quad (\text{A7})$$

These equations are solved in two steps. In the collision step, the variations of the distribution functions are calculated from the collisions as follows:

$$\tilde{f}_i(\vec{r}, t + \delta t) = f_i(\vec{r}, t) + \frac{1}{\tau} [f_i^{\text{eq}}(\vec{r}, t) - f_i(\vec{r}, t)], \quad (\text{A8})$$

where the functions  $\tilde{f}_i$  design the postcollision functions. In the streaming step, the new distributions are advected in the directions of their propagation velocities,

$$f_i(\vec{x} + \vec{c}_i \delta t, t + \delta t) = \tilde{f}_i(\vec{x}, t + \delta t). \quad (\text{A9})$$

The above equations are supplemented by an equation of state, which is obtained by identifying the Navier-Stokes equations with the above equations [55],

$$P(\rho) = \rho c_s^2, \quad (\text{A10})$$

with dynamic viscosity given by

$$\eta = \rho c_s^2 \delta t \left( \tau - \frac{1}{2} \right) \quad (\text{A11})$$

and  $\tau > 1/2$ .

A major advantage of the LBM over other computational fluid dynamics models is its high flexibility for the implementation of geometrically complex boundary conditions. For example, the no-slip boundary condition at a wall or at the surface of an immersed particle simply implies zero velocity at the nodes belonging to the wall surface. This condition can be imposed by requiring that the fluid particles bounce back at the nodes. The fluid forces on the particles are calculated from the balance of momenta at the nodes belonging to the interface [50,58–60].

## 2. Discrete Element Method (DEM)

The DEM is based on the assumption of rigid grains interacting through frictional contacts [61–67]. Newton's equations of motion are integrated for all rigid-body degrees of freedom with simple force laws expressing the normal and friction forces as explicit functions of the elastic deflexion defined from the relative positions and displacements of the

grains at their contact points. We used a linear viscoelastic law for normal forces [68],

$$\vec{f}^n = \begin{cases} k_n \delta_n \vec{n} - \gamma_n \vec{v}_n & \text{if } \delta_n \leq 0 \\ 0 & \text{otherwise} \end{cases}, \quad (\text{A12})$$

where  $\delta_n$  is the overlap,  $\vec{n}$  is the contact normal,  $k_n$  is the normal stiffness, and  $\vec{v}_n$  is the relative velocity along the contact normal.  $\gamma_n$  represents a viscosity parameter with a value that depends on the normal restitution coefficient between grains. The contact is unilateral in the sense that the force vanishes when there is no overlap. For a viscoplastic behavior this unilateral feature is replaced by the condition that negative (tensile) forces cannot be supported by the contact.

For the friction force, we used a linear viscoelastoplastic law as follows:

$$\vec{f}^t = \begin{cases} k_t \vec{\delta}_t - \gamma_t \vec{v}_t & \text{if } |\vec{f}^t| \leq \mu_s f_n \\ -\mu_s f_n \frac{\vec{v}_t}{|\vec{v}_t|} & \text{otherwise} \end{cases}, \quad (\text{A13})$$

where  $\vec{\delta}_t$  is the cumulative tangential displacement since the contact is formed,  $k_t$  is the tangential stiffness of the contact,  $\mu_s$  is the friction coefficient,  $\vec{v}_t = \vec{v} - \vec{v}_n$  is the tangential relative velocity, and  $\gamma_t$  is a viscosity parameter, which depends on the tangential restitution coefficient. The plastic part of this law is simply the Coulomb friction law.

The equations of motion are integrated according to a velocity Verlet scheme [62]. The position vector  $\vec{r}(t + \delta t)$  and rotation vector  $\vec{\theta}(t + \delta t)$  of each grain at the end of a time step  $t + \delta t$  are updated from the position  $\vec{r}(t)$ , rotation vector  $\vec{\theta}(t)$ , velocity  $\vec{V}(t)$ , rotation velocity  $\vec{W}(t)$ , acceleration  $\dot{\vec{V}}(t)$ , and rotational acceleration  $\dot{\vec{W}}(t)$  at time  $t$  by a second-order expansion,

$$\begin{aligned} \vec{r}(t + \delta t) &= \vec{r}(t) + \vec{V}(t) \delta t + \frac{1}{2} \dot{\vec{V}}(t) \delta t^2, \\ \vec{\theta}(t + \delta t) &= \vec{\theta}(t) + \vec{W}(t) \delta t + \frac{1}{2} \dot{\vec{W}}(t) \delta t^2, \end{aligned} \quad (\text{A14})$$

where the velocities  $\vec{V}(t)$  and  $\vec{\theta}(t)$  are calculated from their intermediate values at time  $t + \delta t/2$  given by

$$\begin{aligned} \vec{V}(t + \delta t/2) &= \vec{V}(t) + \dot{\vec{V}}(t) \delta t/2, \\ \vec{W}(t + \delta t/2) &= \vec{W}(t) + \dot{\vec{W}}(t) \delta t/2, \end{aligned} \quad (\text{A15})$$

with

$$\begin{aligned} \vec{V}(t + \delta t) &= \vec{V}(t + \delta t/2) + \dot{\vec{V}}(t + \delta t) \delta t/2, \\ \vec{W}(t + \delta t) &= \vec{W}(t + \delta t/2) + \dot{\vec{W}}_g(t + \delta t) \delta t/2, \end{aligned} \quad (\text{A16})$$

and

$$\begin{aligned} \dot{\vec{V}}(t + \delta t) &= \vec{F}/m, \\ \dot{\vec{W}}(t + \delta t) &= \vec{M}/I, \end{aligned} \quad (\text{A17})$$

where  $\vec{F}$  and  $\vec{M}$  are the total force and torque acting on the grain.

The numerical stability of the above scheme is ensured for a time step below collision duration, which may be estimated for linear elastic interactions to be  $t_c \simeq \pi \sqrt{m/k}$ , where  $k = \max\{k_n, k_t\}$ . The contact dissipation is controlled by dry

friction and viscosity parameters  $\gamma_n$  and  $\gamma_t$ . In order to damp efficiently the elastic oscillations, the viscosity parameters can be increased but not beyond  $\sqrt{mk}$ . Large viscosity parameters lead to small time steps and long relaxation times of long waves. But in the presence of a fluid such oscillations are damped out due to fluid viscosity. The parameter  $\gamma_n$  may be fixed as a function of the normal restitution coefficient for given value of  $k_n$ . But the parameter  $\gamma_t$  should be low enough so as not to mask the effect of fluid viscosity when an immersed granular material is sheared.

Another issue when dealing with a fluid-grains mixture is the effectiveness of lubrication forces. We checked that the lubrication forces are correctly expressed if the  $d/\delta x \geq 16$  [69,70]. The LBM time step  $\delta t_{\text{LBM}}$  is determined from the

lattice spacing and lattice velocity,

$$\delta t_{\text{LBM}} = \frac{\delta x}{c}, \quad (\text{A18})$$

and the relaxation time  $\tau$  in the BGK operator is determined from the fluid viscosity and density,

$$\tau = 3 \frac{\eta}{\rho_f} \frac{\delta t_{\text{LBM}}}{\delta x^2} - \frac{1}{2}. \quad (\text{A19})$$

Note that the LBM time step is generally larger than the DEM time step, which is constrained by the choice of the lattice step and viscosity. This does not harm as far as the hydrodynamic force field evolves more slowly than the grains. This is generally the case for low fluid inertia.

- 
- [1] R. M. Iverson, *Rev. Geophys.* **35**, 245 (1997).
- [2] O. Hungr, S. G. Evans, M. J. Bovis, and J. N. Hutchinson, *Environ. Eng. Geosci.* **7**, 221 (2001).
- [3] F. Legros, *Eng. Geol.* **63**, 301 (2002).
- [4] K. Hewitt, *Am. Sci.* **98**, 410 (2010).
- [5] R. Iverson, *Water Resources Res.* **36**, 1897 (2000).
- [6] D. G. Masson, C. B. Harbitz, R. B. Wynn, G. Pedersen, and F. Lovholt, *Philos. Trans. R. Soc. A* **364**, 2009 (2006).
- [7] R. Day, B. Hawlader, R. Phillips, and K. Soga, in *Proceedings of the International Offshore and Polar Engineering Conference (International Offshore and Polar Engineering Conference, Danvers, MA, 2012)*, pp. 766.
- [8] M. J. Rhodes, *Introduction to Particle Technology* (John Wiley & Sons, Chichester, 1998).
- [9] J. J. Stickel and R. L. Powell, *Annu. Rev. Fluid Mech.* **37**, 129 (2005).
- [10] A. J. Liu and S. R. Nagel, *Jamming and Rheology* (Taylor & Francis, New York, 2001).
- [11] J. S. Chong, E. B. Christiansen, and A. D. Baer, *J. Appl. Polym. Sci.* **15**, 2007 (1971).
- [12] F. Boyer, É. Guazzelli, and O. Pouliquen, *Phys. Rev. Lett.* **107**, 188301 (2011).
- [13] F. Blanc, F. Peters, and E. Lemaire, *J. Rheol.* **55**, 835 (2011).
- [14] A. Schofield and W. C.P., *Critical State Soil Mechanics* (McGraw-Hill, London, 1968).
- [15] D. Wood, *Soil Behavior and Critical State Soil Mechanics* (Cambridge University Press, Cambridge, UK, 1990).
- [16] J. Mitchell and K. Soga, *Fundamentals of Soil Behavior* (Wiley, New York, 2005).
- [17] L. Staron, F. Radjai, and J.-P. Vilotte, *Eur. Phys. J. E. Soft. Matter* **18**, 311 (2005).
- [18] R. M. Iverson, *Math. Geol.* **25**, 1027 (1993).
- [19] M. Pailha, M. Nicolas, and O. Pouliquen, *Phys. Fluids* **20**, 111701 (2008).
- [20] L. Rondon, O. Pouliquen, and P. Aussillous, *Phys. Fluids* **23**, 073301 (2011).
- [21] R. M. Iverson, M. E. Reid, N. R. Iverson, R. G. LaHusen, M. Logan, J. E. Mann, and D. L. Brien, *Science* **290**, 513 (2000).
- [22] A. Taboada, N. Estrada, and F. Radjai, *Phys. Rev. Lett.* **97**, 098302 (2006).
- [23] G. Bossis and J. F. Brady, *J. Fluid Mech.* **155**, 105 (1985).
- [24] M. R. Swift, E. Orlandini, W. R. Osborn, and J. M. Yeomans, *Phys. Rev. E* **54**, 5041 (1996).
- [25] A. Wachs, *Comput. Fluids* **38**, 1608 (2009).
- [26] C. Aidun and J. Clausen, *Annu. Rev. Fluid Mech.* **42**, 439 (2010).
- [27] V. Topin, F. Dubois, Y. Monerie, F. Perales, and A. Wachs, *J. Non-Newtonian Fluid Mech.* **166**, 63 (2011).
- [28] V. Topin, Y. Monerie, F. Perales, and F. Radjai, *Phys. Rev. Lett.* **109**, 188001 (2012).
- [29] D. R. J. Owen, C. R. Leonardi, and Y. T. Feng, *Int. J. Numer. Methods Eng.* **87**, 66 (2011).
- [30] R. M. Iverson, *J. Geophys. Res.* **110**, 2003 (2005).
- [31] F. Radjai and F. Dubois, *Discrete-Element Modeling of Granular Materials* (Iste-Wiley, London, 2011).
- [32] R. M. Iverson, *Water Resources Research* **36**, 1897 (2000).
- [33] X. Wang, H. P. Zhu, S. Luding, and A. B. Yu, *Phys. Rev. E* **88**, 032203 (2013).
- [34] O. Pouliquen, *Phys. Fluids* **11**, 542 (1999).
- [35] F. da Cruz, S. Emam, M. Prochnow, J.-N. Roux, and F. Chevoir, *Phys. Rev. E* **72**, 021309 (2005).
- [36] GDR-MiDi, *Eur. Phys. J. E* **14**, 341 (2004).
- [37] Y. Forterre and O. Pouliquen, *Annu. Rev. Fluid Mech.* **40**, 1 (2008).
- [38] T. Weinhart, R. Hartkamp, A. R. Thornton, and S. Luding, *Phys. Fluids* **25**, 070605 (2013).
- [39] I. Agnolin and J.-N. Roux, *Phys. Rev. E* **76**, 061303 (2007).
- [40] S. Roux and F. Radjai, in *Physics of Dry Granular Media*, edited by H. Herrmann, J. Hovi, and S. Luding (Kluwer, Dordrecht, 1999), pp. 229–235.
- [41] F. Radjai, H. Troadec, and S. Roux, in *Granular Materials: Fundamentals and Applications*, edited by S. Antony, W. Hoyle, and Y. Ding (The Royal Society of Chemistry, Cambridge, 2004), pp. 157.
- [42] S. Taylor, *Soil Science* **86**, 83 (1958).
- [43] L. Rothenburg and R. J. Bathurst, *Geotechnique* **39**, 601 (1989).
- [44] F. Radjai, D. E. Wolf, M. Jean, and J.-J. Moreau, *Phys. Rev. Lett.* **80**, 61 (1998).
- [45] E. Azéma, G. Saussine, and F. Radjai, *Mech. Mater.* **41**, 729 (2009).
- [46] F. Radjai, J.-Y. Delenne, E. Azéma, and S. Roux, *Granular Matter* **14**, 259 (2012).
- [47] R. M. Nedderman, *Statics and Kinematics of Granular Materials* (Cambridge University Press, Cambridge, 1992).
- [48] F. Radjai and V. Richefeu, *Philos. Trans. R. Soc. A* **367**, 5123 (2009).

- [49] E. Azéma, F. Radjai, R. Peyroux, and G. Saussine, *Phys. Rev. E* **76**, 011301 (2007).
- [50] M. Bouzidi, M. Firdaouss, and P. Lallemand, *Phys. Fluids* **13**, 3452 (2001).
- [51] Z. G. Feng and E. E. Michaelides, *J. Comput. Phys.* **195**, 602 (2004).
- [52] Y. T. Feng, K. Han, and D. R. J. Owen, *Int. J. Numer. Methods Eng.* **72**, 1111 (2007).
- [53] Z. Yu and A. Wachs, *J. Non-Newtonian Fluid Mech.* **145**, 78 (2007).
- [54] X. He and L.-S. Luo, *Phys. Rev. E* **55**, R6333 (1997).
- [55] S. Chapman and T. Cowling, *The Mathematical Theory of Nonuniform Gases* (Cambridge University Press, Cambridge, 1970).
- [56] A. Satoh, *Introduction to the Practice of Molecular Simulation* (Elsevier Insights, Amsterdam, 2011).
- [57] P. Bathnagar, E. Gross, and M. Krook, *Phys. Rev.* **94**, 511 (1954).
- [58] K. Iglberger, N. Thürey, and U. Rüde, *Comput. Math. Appl.* **55**, 1461 (2008).
- [59] P. Lallemand and L. S. Luo, *J. Comput. Phys.* **184**, 406 (2003).
- [60] D. Z. Yu, R. W. Mei, L. S. Luo, and W. Shyy, *Progr. Aerospace Sci.* **39**, 329 (2003).
- [61] P. A. Cundall, Ph.D. thesis, Imperial College London, 1971.
- [62] M. P. Allen and D. J. Tildesley, *Computer Simulation of Liquids* (Oxford University Press, Oxford, 1987).
- [63] M. Jean, *Comput. Methods Appl. Mech. Eng.* **177**, 235 (1999).
- [64] J. J. Moreau, in *Powders & Grains 93* (A. A. Balkema, Rotterdam, 1993), p. 227.
- [65] S. Luding, J. Duran, E. Clément, and J. Rajchenbach, in *Proc. of the 5th Chemical Engineering World Congress* (AIChE, San Diego, 1996).
- [66] S. Luding, *Granular Matter* **10**, 235 (2008).
- [67] F. Radjai and V. Richefeu, *Mech. Mater.* **41**, 715 (2009).
- [68] N. V. Brilliantov and T. Pöschel, *Philos. Transact. A Math. Phys. Eng. Sci.* **360**, 415 (2002).
- [69] C. Kunert, J. Harting, and O. I. Vinogradova, *Phys. Rev. Lett.* **105**, 016001 (2010).
- [70] N. Nguyen and A. Ladd, *Phys. Rev. E* **66**, 046708 (2002).